Stochastic influences on pattern formation in Rayleigh-Bénard convection: Ramping experiments

Christopher W. Meyer, Guenter Ahlers, and David S. Cannell
Department of Physics and Center for Nonlinear Science, University of California, Santa Barbara, California 93106
(Received 8 February 1991)

We report on computer-enhanced shadowgraph flow-visualization and heat-flux measurements of pattern formation in convective flows in a thin fluid layer of depth d that is heated from below. Most of the experiments were conducted in a cylindrical container of radius r and aspect ratio $\Gamma \equiv r/d = 10$. The temperature of the top plate of the container was held constant while the heat current through the fluid was linearly ramped in time, resulting in a temperature difference ΔT between the bottom and top plates. After initial transients ended, the reduced Rayleigh number $\epsilon \equiv \Delta T/\Delta T_c - 1$, where ΔT_c is the critical temperature difference for the onset of convection, increased linearly with ramp rate β such that $\epsilon(t) = \beta t$. When time was scaled by the vertical thermal diffusion time, our ramp rates were in the range $0.01 \leq \beta \leq 0.30$. When the sidewalls of the cell were made of conventional plastic materials, a concentric pattern of convection rolls was always induced by dynamic sidewall forcing. When sidewalls were made of a gel that had virtually the same thermal diffusivity as the fluid, pattern formation occurred independent of cell geometry. In the earliest stages the patterns were then composed of irregularly arranged cells and varied randomly between experimental runs. The same random cellular flow was also observed in samples of square horizontal cross section. The results demonstrate the importance of stochastic effects on pattern formation in this system. However, an explanation of the measured convective heat current in terms of theoretical models requires that the noise source in these models have an intensity that is four orders of magnitude larger than that of thermal noise.

I. INTRODUCTION

Many nonlinear dissipative systems subjected to an external stress R will undergo a transition from a spatially uniform state to a state of lower symmetry, with characteristic spatial variation, when R exceeds a critical value R_c [1]. Typical of such systems are Rayleigh-Bénard convection [2,3], rotating Couette-Taylor flow [4,5], electrohydrodynamic convection in nematic liquid crystals [6], dendritic crystal growth [7], flame fronts [8], certain chemical reactions [9], and electric currents in semiconductors [10]. In the ideal system, there is a bifurcation point $R = R_c$ at which an exchange of stability occurs between the spatially uniform state and the state with spatial variation. Above R_c, the uniform state is still a solution of the equations of motion of the system, but it is unstable. Thus, if R is changed from below to above R_c, a finite perturbation of the ideal system is required if it is to evolve to the stable state of lower symmetry in a finite length of time.

In this paper we address the question of how a real physical system evolves from the unstable to the stable state of broken spatial symmetry. Of particular interest to us was whether stochastic effects ever play a significant role in this pattern evolution. Such effects have been studied both theoretically [11,12] and experimentally [13,14] for the onset in a laser. However, that work did not involve a spatially extended system in which a continuum of (or at least very many) modes can become unstable, and thus a single-mode description without spatial variation turned out to be sufficient to explain the experimental observations. Stochastic effects have been considered theoretically for spatially extended hydrodynamic systems, in particular for Rayleigh-Bénard convection, by a number of authors [15–19], but their experimental study so far has been largely inconclusive for macroscopic systems. Evidence for stochastic effects has been found recently, however, in a study of sidebranching in dendritic crystal growth [20].

The particular example of our experimental study is the Rayleigh-Bénard (RB) system [2,3,21]. It consists of a horizontal layer of fluid (water in this case) which is heated from below and cooled from above. For this case the stress parameter R is the Rayleigh number, which is proportional to the temperature difference across the layer. In the presence of gravity, the purely conducting state loses stability to a state with a finite fluid velocity when R exceeds its critical value. The velocity field has a characteristic spatial pattern, and thus the full translational symmetry of the conduction state is broken. For $R > R_c$, the steady-state amplitude of the convecting state evolves continuously from zero as R increases [22], and the bifurcation from conduction to convection therefore is said to be forward. We believe that our results are typical for systems with forward bifurcations. We chose our particular system because the externally controlled parameters and the boundary conditions can be specified and controlled in the laboratory with very high accuracy in this case [23] and because the full equations of motion are well known.

We report on experimental results of heat-current measurements and flow visualization, which were obtained while R was varied monotonically in time from below to above R_c. In these experiments the convective heat current evolved to macroscopic values and a flow pattern

became observable only some time after R_c had been exceeded. This delay, as well as the quantitative details of the heat-current evolution and the nature of the pattern which first forms, gives information about the nature of the perturbations that cause the system to evolve towards its stable finite-amplitude state. Similar experiments had been done before by Ahlers *et al.* (to be referred to as ACHS henceforth) [18], but in that work there was no flow visualization and the heat-current measurements by themselves did not give definitive answers about the nature of the perturbations.

We find that the pattern which grows depends on the nature of the sidewalls of the sample. In our cylindrical geometry with water as the fluid, concentric convecting rolls are induced when the walls are made of typical plastic materials. This forcing of the pattern by the walls is a dynamic effect. During the time-dependent heating of the cell bottom, the temperature gradient in the wall evolves at a rate which differs from that in the fluid because the two materials have different thermal diffusivities. Therefore, there is a horizontal temperature gradient in the fluid near the wall, and such a gradient is known to induce convective flow even when it is quite small. This dynamic sidewall forcing has been considered previously as a possible explanation of the earlier experiments [18], and its size has been calculated from the thermal properties of the fluid and the walls [24]. Our visualizations, as well as our measured currents, were quite consistent with this deterministic effect when we used conventional sidewalls.

Although dynamic sidewall forcing has turned out to be an interesting problem in itself, it was our goal to reduce deterministic sources of the convective onset to a negligible level so that finally stochastic effects due to external noise sources might become observable. We reduced dynamic sidewall forcing by making the walls of a material with thermal properties which are virtually the same as those of the fluid. Such a material is a gel, consisting of 95% of the fluid (water) and 5% of polyacrylamide by weight, which has nearly the same diffusivity as the fluid. Nonetheless, the gel had enough rigidity to maintain its shape in the presence of gravity and of the flow field adjacent to it. With this sidewall the nature of the convective onset was dramatically modified. The evolving pattern initially consisted of randomly positioned cells. It had no noticeable relationship to the shape of the walls. The positions of the cells had no geometric regularity, and were not reproducible from one experimental run to the next. This type of pattern occurred in cells of circular as well as of square horizontal cross section. We believe that this convective onset is provoked by spatially and temporally random perturbations, i.e., by stochastic forcing. This conclusion is supported also by an analysis of the time dependence of the evolving convective heat current. This time dependence agrees much better with stochastic models [18,25,26] of the convective onset than with a deterministic one.

The analysis of the current also gave information about the intensity of the noise source which is required in the models to explain the experimentally observed onset in terms of the stochastic effects. It turns out that this intensity is four orders of magnitude larger than the intensity of thermal noise at room temperature (i.e., the rms amplitude is about a factor of 100 larger). We searched for likely experimental noise sources, but found that changes in the experiment that seemed most likely to affect experimentally induced noise did not alter our results. Thus, we unfortunately have to report at this time that we do not know the origin of this factor of 10^4. Brief reports on the work which we discuss in detail in this paper have already been published elsewhere [27–29].

In addition to the measurements with temporal ramps of the current, we also did experiments in which the current was modulated time periodically [27]. In that case R was periodic in time, and varied from below to above R_c and below again during each cycle. Once during each cycle, the pattern grew from a microscopic, unobservable amplitude to a recognizable pattern, and then decayed again. Results obtained through this work also revealed the importance of stochastic effects in pattern formation. Within the framework of the same stochastic models that we use in the present paper, they were consistent with the noise strength inferred from the ramping experiments. The results of the modulation work will be presented in detail in a subsequent paper.

The remainder of this paper is organized as follows: In Sec. II we describe our apparatus and the experimental method. It includes a discussion of the flow visualization, of the computer analyses performed on the images, and of the heat-flux measurements. Section III contains a description of experimental procedures, and of the determination of the convective heat current from the primary experimentally measured quantities. In Sec. IV we discuss the theoretical models that were used to analyze the results for the current. These include a deterministic and a stochastic single-mode approximation [18,25] as well as a more rigorous two-dimensional stochastic model [25] based on the Swift-Hohenberg [17] equation. In Sec. V we present our results. Some details of our image processing are presented in an appendix.

II. APPARATUS AND EXPERIMENTAL METHODS

A. The fluid

The fluid used was water near 25.6 °C with thermal expansion coefficient $\alpha=2.63\times10^{-4}$ K^{-1}, specific heat $C_p=4.172$ J/g K, thermal conductivity $\Lambda=6.07\times10^{-3}$ W/cm K, kinematic viscosity $\nu=8.83\times10^{-3}$ cm^2/sec, and thermal diffusivity $\kappa=1.47\times10^{-3}$ cm^2/sec. The Prandtl number is $\sigma\equiv\nu/\kappa=6.0$. The water was distilled, fed through a Milli-Q ion-exchange system (Millipore Co.), and boiled before it was placed in the cell. The fluid layer was 0.318 ± 0.002 cm thick, resulting in a predicted value of $\Delta T_c=2.493$ K and $t_v\equiv d^2/\kappa=68.8$ sec. When $\Delta T=\Delta T_c$ in such a layer, the parameter Q that describes the extent of the departure from the Oberbeck-Boussinesq (OB) approximation [30,31] is $Q=-0.416$. For this value of Q, a pattern of rolls is predicted [30] to be unstable to hexagons only for the small range $0\leq\epsilon\leq2.2\times10^{-3}$, and hexagons are predicted to be unstable with respect to rolls for $\epsilon\geq7.7\times10^{-3}$. Experi-

mentally, we have never detected a hexagon pattern immediately above the threshold, and therefore we believe that this system conforms very well to the OB approximation.

B. The apparatus

Our apparatus is an improved version of that designed by Steinberg *et al.* [23]. A schematic diagram of the convection cell and its container is shown in Fig. 1. The top plate was a single-crystal sapphire disk with a diameter of 10.16 cm and a thickness of 0.318 cm (Crystal Systems). The c axis was oriented perpendicular to the disk. The plate was flat to within 5 μm. The bottom plate was a copper disk with a diameter of 8.9 cm and a thickness of 0.635 cm, plated on its upper surface with 0.015 cm of nickel. The nickel was lapped and polished to a mirror finish. It was flat to within 2 μm. A 90-Ω metal-film heater with a diameter of 8.9 cm (Minco Products) was attached with adhesive to the lower surface of this plate to provide it with uniform heating. A 0.08-cm-diam vertical hole, located at 0.30 cm from the outer edge of the plate, was drilled through the plate to provide an outlet for the water when it expanded. The diameter of this hole was expanded to 0.16 cm in the lower 0.2 cm of the plate; a copper nozzle was epoxied (Stycast 1266) inside this region. A Tygon tube was attached to it, exited the main apparatus, and terminated in a reservoir of water.

For some experiments we replaced the sapphire top with one made of copper 0.64 cm thick with 0.05 cm of acrylic glued to its upper surface. This top served to greatly reduce the magnitude of any temperature fluctuations imposed on the fluid layer through the top plate. A thermistor (Fenwal GA51M2) embedded in the copper provided a very precise measure of its temperature.

The temperature of the bottom plate was measured with a Fenwal GA51M2 (≈ 100 kΩ at room temperature) thermistor. The thermistor was epoxied into a hole that was 0.2 cm in diameter, 3.5 cm deep, and drilled radially inward from the side at midheight of the plate. The first 5 cm of the thermistor leads were placed in good thermal contact with the plate.

Three different sidewall designs were used in these experiments. Two of them were cylindrical and one was square. We will describe only one sidewall design here; the rest were modifications of it and will be described later. One circular sidewall was made of high-density polyethylene. It had an inner diameter of 6.36 cm, an outer diameter of 8.6 cm, and a thickness of 0.318 cm, resulting in an aspect ratio of $\Gamma = 10.0$. The cell was sealed with a Buna-N O ring which had been cleaned by wiping with ethyl alcohol.

As shown in Fig. 1, a small channel of height 0.13 cm and width 0.25 cm was located in the bottom side of the sidewall. The bottom boundary of the sidewall nearest the cell area was raised by ≈ 0.10 mm to allow the water to flow between the cell and the channel. The bottom-plate fill hole mentioned above was positioned underneath the channel. Through this arrangement, the relatively large flow velocities that exist in the vicinity of the fill hole when the fluid expands under time-dependent heating occurred in a region outside of the active cell area. In earlier experiments we had found that the convective flow pattern emerging when ϵ was increased above its threshold consisted of circular rolls centered around the fill hole when this hole was located in the active area of the cell. This effect is illustrated in Fig. 2, which shows the shadowgraph image of a pattern emerging from the conduction state after ϵ was ramped through zero. Both sidewall and fill-hole forcing are noticeable in this case.

The cell was located inside a cylindrical stainless-steel container with a diameter of 16.3 cm and a depth of 6.4 cm. The sapphire plate was mounted in a stainless-steel plate and sealed with an O ring (not shown). The outer edge of the bottom copper plate was in contact with an acrylic ring of inner diameter 8.6 cm, outer diameter 12.7 cm, and thickness 1.0 cm. The ring was attached to the steel plate by six stainless-steel screws of 4 mm diam and clamped the cell together. The remainder of the container volume was filled with thermally insulating Ensolite foam rubber (Cascade Designs) with thermal conductivity [32] $\Lambda_r \approx 5\times 10^{-4}$ W/cmK, which insured that nearly all the heat applied to the copper plate flowed through the fluid or sidewall.

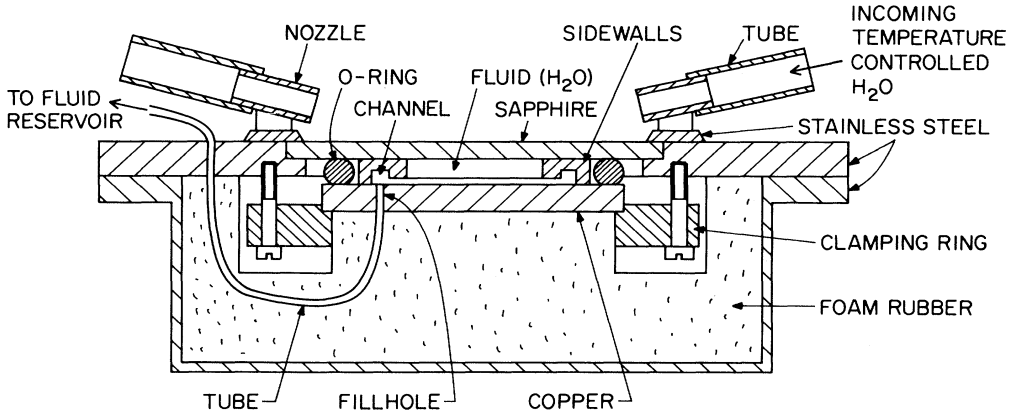

FIG. 1. Schematic diagram of the convection cell and its container, including one of the sidewall designs.

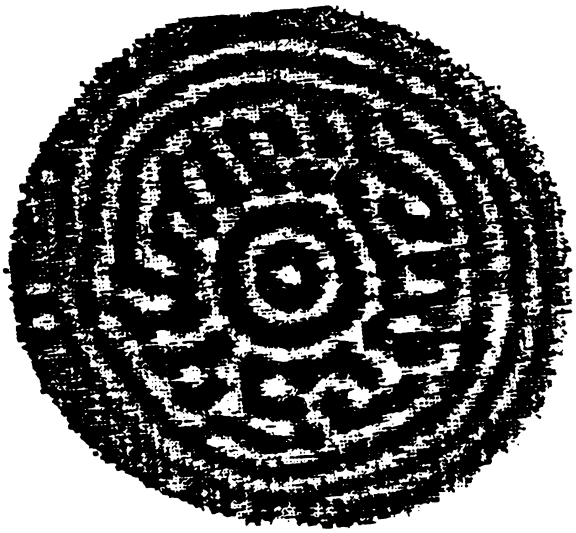

FIG. 2. Emerging convection pattern showing both dynamic sidewall forcing, and forcing due to flow out through a small filling hole in the cell center.

The sapphire plate was held at a constant temperature through contact with a flowing temperature-controlled stream of water. A flow distributer consisting of eight nozzles of inner diameter 0.8 cm directed the water onto the plate with a flow volume of approximately 200 cm^3/sec. The nozzles were mounted equally spaced on a ring that was attached to the top plate of the container, as shown in Fig. 1. They pointed radially inward towards the sapphire plate at a radius of $r \approx 2.25$ cm. Although the flow distributer provided efficient removal of the heat passing through the plate, the temperature of the plate increased slightly when a heat current passed through the cell. A thermistor probe (Fenwal GA51M2) was therefore placed directly on top of the plate to measure its temperature. It rested above the sidewall during the experiments (so that it would not interfere with the flow visualization), but could be moved along the diameter of the plate at other times to measure horizontal temperature variations. When 5×10^{-2} W/cm^2 flowed through the cell (approximately $\dot{Q}_c$), we measured a temperature variation across the plate of 10 mK. The temperature of the plate was at its minimum value at $r \approx 2.25$ cm, and increased monotonically with larger and smaller r. The average temperature was ≈ 30 mK higher than that measured when no heat flowed through the cell.

The cylindrical container was located in the center of a large rectangular stainless-steel tank, as shown in Fig. 3. The tank had a length of 30 cm, a width of 25 cm, and a depth of 13 cm, and was filled with flowing temperature-controlled water. Its walls were covered on the outside by a 2.5-cm-thick layer of foam rubber. The container was raised from the bottom of the tank by three hollow, vertical stainless-steel tubes of length 7.6 cm. The container was held firmly in place by its own weight. An optically flat glass window of diameter 10 cm and thickness 5 mm was mounted with epoxy (Stycast 1266) in the top plate of the tank in the area above the convection cell. The temperature-controlled water entered an entrance chamber of the tank, and from there was distributed via eight Tygon tubes to the nozzles of the flow distributor. The exiting water was recirculated to the entrance through 2.5-cm inner-diameter tubes by means of a pump.

The temperature of the bath water was regulated using a method similar to that of Lunacek and Cannell [33] and Haller *et al.* [34]. A heat exchanger placed in the circu-

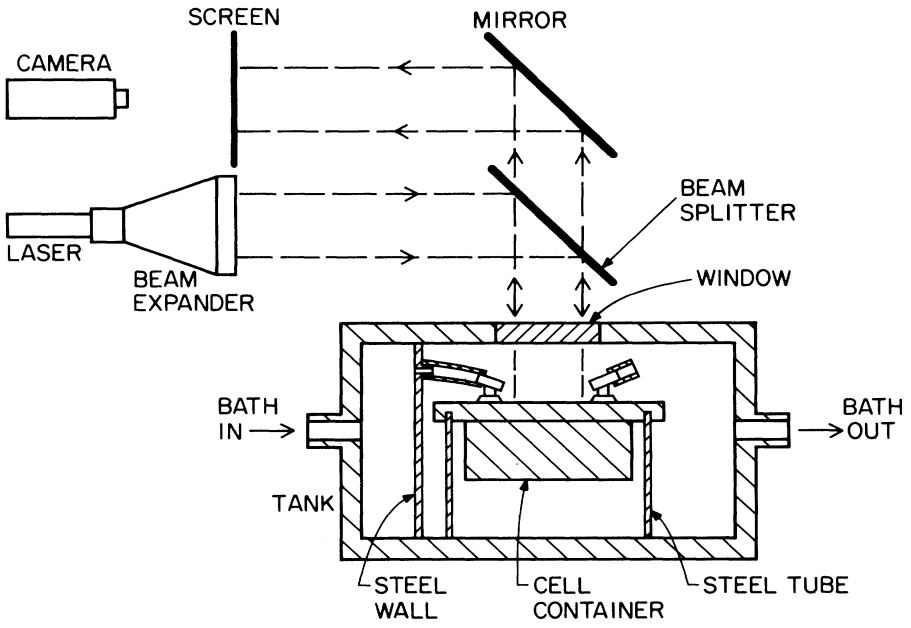

FIG. 3. Schematic diagram of the apparatus, including the cell container, tank, and flow-visualization arrangement.

lation system removed heat from the water at a roughly constant rate. A thermistor in contact with the water in the entrance chamber of the tank, and a heater consisting of 2.5 m of AWG 30 teflon-insulated copper wire arranged in a random dense tangle and placed in the 2.5-cm inner-diameter tube immediately upstream of the entrance chamber, were used to control the bath temperature. This temperature fluctuated with peak-to-peak variations of 1 mK. When averaged over these fluctuations, it did not drift noticeably. With a constant heat current through the cell, the bottom-plate temperature was observed to be stable to within 0.2 mK over periods of many days.

All experiments were automated, using an IBM PC-XT computer. The computer controlled the power applied to the heater at the bottom plate of the convection cell through use of a 12-bit digital-to-analog converter (Tecmar Labmaster), whose output voltage was divided so as to be within an appropriate range and then served as input to a power amplifier (Hewlett-Packard 6024A). The maximum power which could be applied to the heater was 10 W and the minimum step in $\dot{Q}$ around $\dot{Q}_c$ was $\Delta\dot{Q}\cong 3$ mW. The power was measured separately by determining the current passing through the heater. The current was determined by measuring the voltage across a reference resistor with a $5\frac{1}{2}$ digit multimeter. The temperatures of the bottom and top plates were determined by measuring the resistance of their respective thermistors with similar multimeters. These multimeters were interfaced to the computer using the IEEE-488 bus, enabling simultaneous measurements of all quantities at specified intervals.

C. Flow visualization

We used the shadowgraph method to visualize the flow patterns. To our knowledge, this experimental technique was first applied to convection by Silveston [35,36] and has been used extensively by Chen and Whitehead [37] and by Busse and Whitehead [38]. It detects horizontal temperature variations in the fluid. A theoretical description of the shadowgraph method has been provided recently by Jenkins [39] and by Rasenat *et al.* [40]. In our system, which is shown schematically in Fig. 3, a uniform parallel light beam was directed down into the cell, where it was reflected by the mirror surface of the bottom plate up to a translucent screen above the apparatus. It was observed by a Nuvicon video camera (Panasonic). A beam splitter and a mirror were located as shown in the figure. The image on the screen provided a top view of the convection pattern. It contained dark and bright regions, where dark (bright) corresponded to up-flow (down-flow). The video camera was interfaced to the computer, where an image from the camera could be captured with 8-bit resolution using a video-capture card (Chorus Data Systems, Inc.), and subsequently stored in computer memory. A 256×256 8-bit pixel image could be captured in 0.25 sec.

The light source was a 5-mW He-Ne laser. The beam was focused on a rotating frosted-glass wheel within a beam expander using a 2.5-mm focal-length lens, and collected after transmission by an objective lens of focal length 0.25 m. This lens recollimated the beam with a diameter of 15 cm. The purpose of the wheel was to weaken the spatial coherence of the laser beam, thereby reducing undesirable interference fringes in the image. It rotated at 10 Hz, and the distance of the beam from the center of rotation was 3 cm. A narrow-band 6328-Å interference filter (Melles-Griot) was placed over the camera lens to virtually exclude room light.

Earlier shadowgraph studies [35–38] had concentrated on Rayleigh numbers well above the threshold, where the shadowgraph signal is strong. We wanted to detect the patterns very close to the convective onset, and therefore used digital image-enhancement techniques. In processing the images, we used a background division and rescaling method and an image printing method which have been described elsewhere [23]. Background division essentially eliminated large-scale variations in the intensity which were caused by spherical aberration from the lenses as well as by slight tarnishing of the bottom-plate mirror. The image enhancement obtained through background division alone is illustrated in Fig. 4, where an unprocessed image is shown in Fig. 4(a) and the image after background division and rescaling is shown in Fig. 4(b).

Rapid evolution of patterns precluded averaging several images; however, in some applications the noise in single images was reduced by spatial filtering. A two-dimensional Fourier transform of the matrix of pixels composing the background-divided image was performed. As an example, the low-wave-vector portion (a 32×32 matrix) of the magnitude of the Fourier transform of the image in Fig. 4(b) is shown in Fig. 4(c), where the darker pixels correspond to those with a higher magnitude. The information pertaining to the convection pattern is contained inside a circle centered at $k=0$ with a radius slightly larger than k_c. The rest of the Fourier transform corresponds to noise. When filtering the image, we left unchanged all the Fourier-transform pixel values for $k<k_{\rm cut}$, where $k_{\rm cut}$ was adjustable but slightly greater than k_c (we typically used $k_{\rm cut}=1.3k_c$). Above $2k_{\rm cut}$, the pixel values representing the magnitude of the transform were all set to zero. For $k_{\rm cut}\le k<2k_{\rm cut}$, they were decreased through multiplication by the smoothing function

$$I(k)=I_0(k)\cos^2\left[\frac{\pi}{2}\left[\frac{k}{k_{\rm cut}}-1\right]\right]. \tag{2.1}$$

Here, $I_0(k)$ is the original transform magnitude value, and $I(k)$ is its value after spatial filtering. Figure 4(d) shows the contents of Fig. 4(c) after the filtering process. The inner circle is drawn at $k=k_{\rm cut}$ and the outer circle at $k=2k_{\rm cut}$. Since this figure just shows the low-wave-vector portion of the Fourier transform (FT), it only displays a small number of the transform pixel values that were set to zero. The filtered image, Fig. 4(e), is obtained from an inverse Fourier transform and rescaling. The roll pattern is considerably easier to identify now that the high-wave-vector noise has been filtered out.

The image shown in Fig. 4 is the central portion of a full convection pattern. Full patterns, such as those shown in Fig. 10 below, were also filtered, but some extra steps had to be taken. Pixels within the image matrix but outside the circular pattern were normally [23] assigned the value 0 and are displayed white. For the Fourier transform, these background pixels were assigned a value corresponding to the average pixel value within the pattern. After the spatial filtering had been performed, the background pixels were reassigned the value 0.

D. Pattern analysis

Two types of measurements were made on the images. The mean wave vector $\bar{k}$ and the variance σ_k^2 of the wave vector were determined from the Fourier transform. For $\bar{k}$ we used

$$\bar{k}=\frac{\sum_{i,j} k_{ij} I_{ij}}{\sum_{i,j} I_{ij}} . \tag{2.2}$$

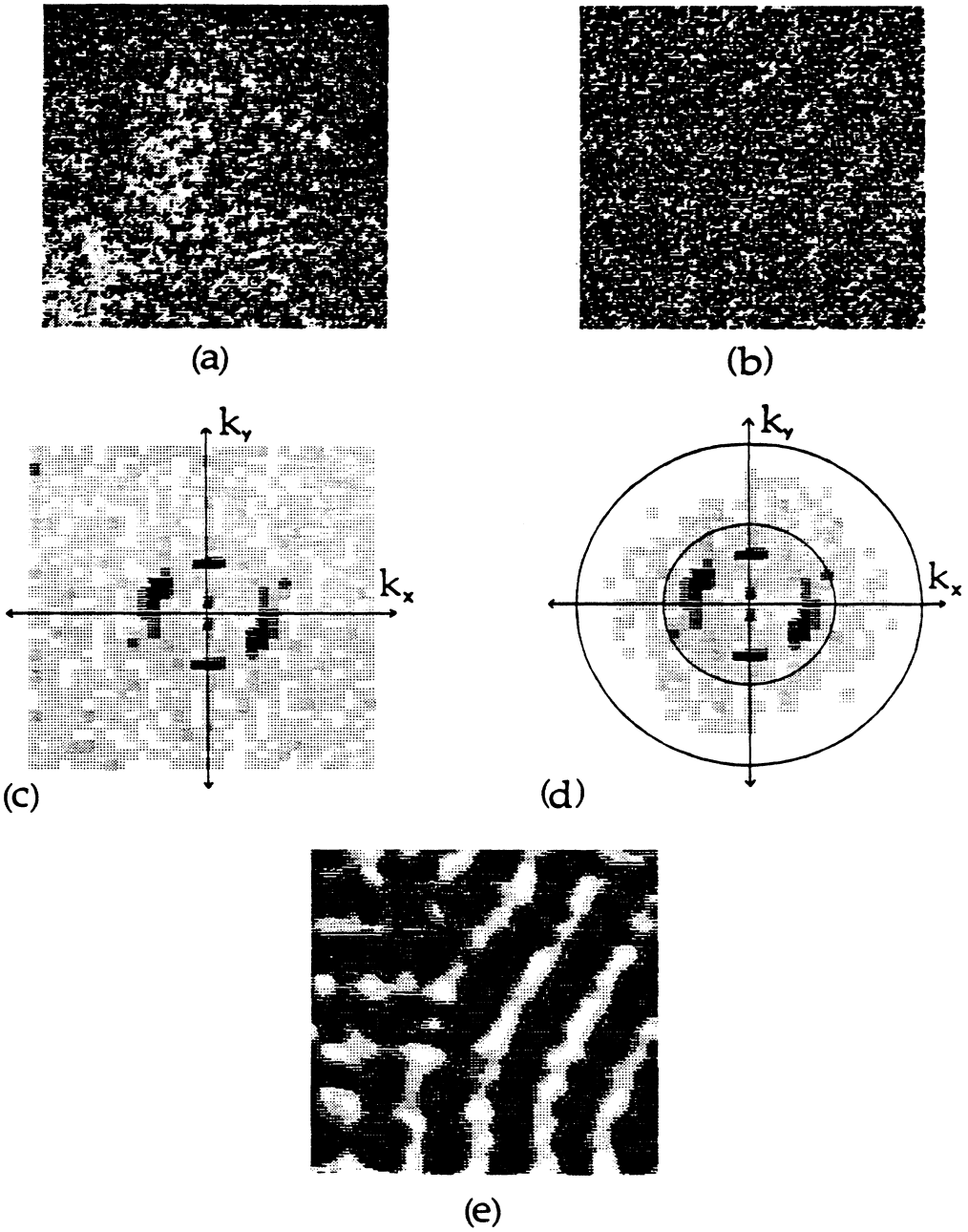

FIG. 4. Image-processing techniques used on a weak convection pattern. (a) Unprocessed image. (b) Same image after background division. (c) Central portion of Fourier transform of background-divided image. (d) Same Fourier transform after spatial filtering. (e) Image after spatial filtering [inverse transform of (d)].

Here, k_{ij} is the wave number and I_{ij} is the magnitude of the Fourier transform, and the indices refer to the elements of the matrix comprising the transform. The variance was calculated from

$$\sigma_k^2 = \frac{\sum_{i,j}(k_{ij}-\bar{k})^2 I_{ij}}{\sum_{i,j} I_{ij}} . \tag{2.3}$$

These results were scaled by the theoretical value of the critical wave number [41] $k_c = 3.116$. When calculating $\bar{k}$ and σ_k, all elements I_{ij} whose corresponding values of k_{ij} were outside the range $0.5k_c \leq k_{ij} < 1.4k_c$ were assigned the value 0.

The second quantity used to characterize a pattern was the total length B of the boundary separating regions of up-flow and down-flow. In order to measure B, all pixels whose value was above (below) the mean pixel value were represented as white (black). An algorithm was developed to measure the total length of the boundary between black and white regions (see the Appendix). We normalized B so that for a straight roll pattern, $B = 1$. A cellular pattern, by contrast, was observed to have $B \approx 1.2$. The value of B therefore provided a measure of the cellularity of the pattern.

E. Heat-flux measurements

1. Calculation of convective heat current under steady heating

The temperature difference ΔT was directly measured with thermistor probes located in the bottom plate, and in the bath immediately above the top plate of the convection cell. The sapphire top plate had a thermal conductivity of 0.35 W/cm K, which is 60 times that of water at 25.6 °C, and had a thickness very nearly equal to that of the fluid layer. The plate therefore had a temperature difference across it that was 1.7% of the total ΔT. A small temperature difference also existed between the top of the sapphire plate and the controlled bath across a boundary layer of thickness ≈ 1 mm immediately above the plate. The temperature measured by the thermistor in the bath, whose head was also ≈ 1 mm thick, was a spatial average of that in the boundary layer. Because of these additions to the temperature difference, measurements of ΔT were systematically high by 2–3 %. We will discuss the possible effects of these systematic errors later.

The experimentally measured total heat flux $\dot{Q}$ flowed partly through the fluid and partly through the sidewalls and foam-rubber insulation (see Fig. 1). In the absence of convection, and at steady state, the flux is purely conductive, and may be written

$$\dot{Q} = \dot{Q}^{\,\mathrm{cond}} = \frac{A_f \Lambda_f}{d}\Delta T + g\Delta T , \tag{2.4}$$

where A_f, Λ_f and d are the cross-sectional area of the fluid layer, its thermal conductivity, and its thickness, respectively, and g is the thermal conductance of the sidewall-foam combination. In order to determine g, we measured the ΔT resulting from an imposed $\dot{Q}$ for ΔT typically 20% less than ΔT_c, and used the value of Λ_f corresponding to the mean temperature of the fluid layer.

Under steady-state conditions, the convective heat flux $\dot{Q}^{\,\mathrm{conv}}$ is the difference between the total heat flux and the conductive portion:

$$\dot{Q}^{\,\mathrm{conv}} = \dot{Q} - \dot{Q}^{\,\mathrm{cond}} , \tag{2.5}$$

and is therefore determined by the measurements of $\dot{Q}$ and ΔT, once the constant g has been measured. The dimensionless heat current j^{conv} is the ratio of $\dot{Q}^{\,\mathrm{conv}}$ to the heat current conducted through the fluid for $\Delta T = \Delta T_c$, i.e., to 2.635 K. The Nusselt number N is the ratio of the total heat current through the fluid to that which would be conducted by a quiescent fluid under the same conditions. Consequently, j^{conv} and N are related by

$$j^{\mathrm{conv}} = (N-1)(1+\epsilon) , \tag{2.6}$$

with

$$\epsilon \equiv \Delta T/\Delta T_c - 1 = R/R_c - 1 , \tag{2.7}$$

which is valid [42] for a Boussinesq [43,44] system and which is an excellent approximation for our case.

2. Static heat-flux measurements

New static heat-flux measurements were made every time the cell was reassembled. Measurements of ΔT_c typically varied by 1–2 % even when the same sidewall was used. This was due to the sensitivity of ΔT_c to d, which may vary slightly from one cell assembly to the next. Shown in Fig. 5 as solid circles are static measurements obtained while using the high-density polyethylene sidewall illustrated in Fig. 1. We measured $\Delta T_c = 2.635$ °C, which is 6% higher than that predicted by theory for a laterally infinite system. As discussed in Sec. II E 1, 2–3 % may be due to the systematic errors in measurements of ΔT. An additional 1% may be attributed to uncertainties in the cell thickness. Systematic errors in the thermistor calibration [45] and the finite size of the cell explain the remainder. The curve for $\epsilon < 0$ is $j^{\mathrm{conv}} = 0$. That for $\epsilon \geq 0$ is described by the function

$$j^{\mathrm{conv}} = \frac{-g_3 + (g_3^2 + 4g_5\epsilon)^{1/2}}{2g_5} , \tag{2.8}$$

where $g_3 = 0.832$ and $g_5 = -0.104$ are best-fit values to this function over the range $0 \leq \epsilon < 0.6$. Our reason for choosing this functional form will be explained in Sec. IV. The value of g_3 is theoretically predicted [22] to be 0.699 for an infinite system of straight rolls and a Prandtl number $\sigma = 6.0$. The measured value exceeds the predicted value by 19%. Only a small part of this discrepancy can be attributed to experimental errors, and most of it we believe to be due to the finite system size, and to the disorder in the pattern which is provoked by sidewalls. Similar high values of g_3 have also been obtained in other experiments [42,46–49].

III. EXPERIMENTS

A. Experimental procedure

We kept the bath temperature constant and ramped the power applied to the bottom plate linearly with time so that ϵ increased from below to above $\epsilon=0$. The power varied as

$$\dot{Q}/\dot{Q}_c=\beta'(t-t_0)\ . \tag{3.1}$$

Here, β' is the ramp rate and t_0 is chosen so that the time t is equal to zero when $\epsilon=0$. We performed these experiments for $0.01\leq\beta'\leq 0.32$. All ramping experiments began with $\epsilon=-1$, with the exception of those with $\beta'=0.02$ and $\beta'=0.01$, where the experiments began at $\epsilon=-0.6$ and $\epsilon=-0.2$, respectively. We allowed the system to equilibrate for 30 min ($26t_v$) at these values of ϵ before the beginning of each ramp. Measurements of $\Delta T(t)$ were made and frequent shadowgraph images of the convective pattern were taken during each experimental run.

Although $\dot{Q}$ was ramped linearly, ϵ did not increase linearly for the entire run. Two effects accounted for this. First, the large heat capacity of the copper bottom plate caused there to be an initial transient period before the temperature of the plate increased linearly with time. Secondly, once convection began, the effective thermal conductivity of the fluid layer increased, causing a decrease in the rate of increase of ϵ with time. These two effects are illustrated in Fig. 6, which plots $\dot{Q}/\dot{Q}_c$ (dashed curve) and $\Delta T/\Delta T_c=\epsilon+1$ (solid curve) as a function of time for $\beta'=0.32$. Note that the critical temperature difference was passed at $t-t_0\approx 5.2$, while noticeable convection did not occur until $t-t_0\approx 6.5$.

For the runs with $\beta'\leq 0.16$, the initial transient period was short when compared with the duration of the run. For larger β', however, the fraction of the run involving this period became significant. Finally, at $\beta'=0.30$, the increase of ϵ approached linearity only at $\epsilon=0$. Because of the transient period, we shall define a second ramp rate which is related to the increase of ϵ rather than that of the heat current and which we will use primarily throughout the remainder of this paper:

$$\beta\equiv\left[\frac{d\epsilon}{dt}\right]_{\epsilon=0}\ . \tag{3.2}$$

For small β', we found $\beta=\beta'$. For larger β', however, $\beta<\beta'$ because the transient period had not completely ended.

B. Determination of the convective heat current

The time-dependent convective heat current $j^{\rm conv}(t)$ was experimentally determined from measurements of $\dot{Q}(t)$ and $\Delta T(t)$. The method was similar to that used in Ref. [18]. From conservation of energy, $\dot{Q}^{\rm conv}$ must be the power that cannot be accounted for by thermal conduction through the fluid and sidewall and by the heating of the cell and its contents:

$$\dot{Q}^{\rm conv}(t')=\dot{Q}-\frac{(\Lambda_f A_f+\Lambda_s A_s+\Lambda_r A_r d/d_r)}{d}\Delta T - \left[C_B+\frac{C_f+C_s+C_r}{3}\right]\frac{dT^b}{dt'}\ , \tag{3.3}$$

where C_B, C_f, C_s, and C_r are the heat capacities of the bottom plate, fluid, sidewall, and foam, respectively, and t' is the unscaled time. The conductive term and the term involving $(C_f+C_s+C_r)/3$ are obtained from the solution to the heat-conduction problem of a horizontal slab where the top-boundary temperature is held constant and the bottom-boundary temperature is increased linearly with time. For the experiment, this term represents an approximation, since the bottom-plate temperature does not always increase linearly (see Fig. 6). The approximation, however, is quite good, because the ramp rate did not change dramatically over short time intervals. The dimensionless convective heat current $j^{\rm conv}(t)$, as a function of the scaled time $t\equiv t'/t_v$, is obtained from Eq. (3.3), as the ratio of $\dot{Q}^{\rm conv}(t)$ to the flux conducted through the fluid at $\Delta T=\Delta T_c$ [see Eq. (2.4)]. Consequently, $j^{\rm conv}(t)$ is given by

$$j^{\rm conv}=\left[\frac{\dot{Q}}{\dot{Q}_c}-\frac{\Delta T}{\Delta T_c}-\frac{c_1}{\Delta T_c}\frac{dT^b}{dt}\right]\left[1+\frac{gd}{\Lambda_f A_f}\right]\ , \tag{3.4}$$

where

$$c_1=\frac{C_B+(C_f+C_s+C_r)/3}{t_v}(g+\Lambda_f A_f/d)\ . \tag{3.5}$$

Since the top plate temperature increased by only about 30 mK by the time $\Delta T=\Delta T_c$, we set $dT^b/dt=d(\Delta T)/dt$ to obtain a good approximation $j_0^{\rm conv}(t)$ to the convective

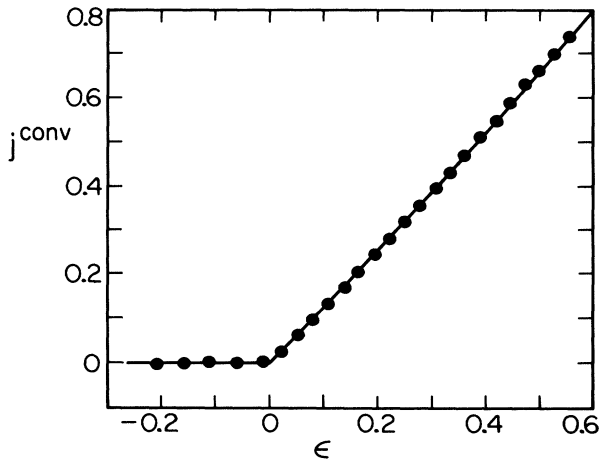

FIG. 5. Measurements of $j^{\rm conv}$ as a function of ϵ under steady heating (shown as solid circles). The curve for $\epsilon<0$ is $j^{\rm conv}=0$. The rest of the curve is a least-squares fit to Eq. (2.8) through the points over the range $0\leq\epsilon<0.6$.

heat current,

$$j_0^{\rm conv}(t)=\left[\frac{\dot{Q}}{\dot{Q}_c}-\frac{\Delta T}{\Delta T_c}-\frac{c_1}{\Delta T_c}\frac{d\Delta T}{dt}\right]\left[1+\frac{gd}{\Lambda_f A_f}\right], \tag{3.6}$$

in terms of measured quantities.

The time derivative of ΔT was obtained from the measured $\Delta T(t)$. From Eq. (3.5) we estimated the value of c_1 to be 2.45. When calculating $j_0^{\rm conv}$, however, we used a value of c_1 which for the particular run yielded $j^{\rm conv}\equiv 0$ when $\epsilon=0$. This value of c_1 was 2.55 at $\beta=0.01$, and decreased monotonically with β to $c_1=2.28$ at $\beta=0.30$.

Ideally, the calculated value of $j^{\rm conv}$ should have been zero during the entire period before the onset of convection. Instead, it increased slightly during the runs, particularly during those with higher ramp rates. In order to make accurate measurements of $j^{\rm conv}$, we felt that it was important to understand this problem and to make corrections for it. We therefore replaced the water in our cell with a gel of 95% water and 5% polyacrylamide. With this arrangement the cell had almost exactly the same thermal properties (the thermal conductivity of the gel was measured to be that of water to within 3%) but could not convect. We performed the same ramping experiments on this system as were done on the cell containing water. Shown in Fig. 7 are the results for the apparent heat current $j_0^{\rm conv,g}$ in the presence of the gel for two ramp rates. The plot of Fig. 7(a), with $\beta=0.02$, reveals the problem: The existence of a very long initial transient period which lasted $\approx 20t_v$. We believe that this is due to long-lived transients in the heat flow through the foam below the cell. The length of the transient period is consistent with the large thermal diffusion time of the foam. For runs with small ramp rates, such as the run of Fig. 7(a), the transient period ended before the convective onset at $t=0$, and so above this point $j_0^{\rm conv,g}$ was always zero. For runs with higher ramp rates, such as the run of Fig. 7(b) (which was done with $\beta=0.30$), this was not the case, and $j_0^{\rm conv,g}$ increased with time. The existence of the transient may explain the variation of the measured value of c_1 with β. Note that $j_0^{\rm conv,g}$ is small compared to typical total convected currents, such as those shown, for instance, in Fig. 10 below. When making measurements of $j^{\rm conv}(t)$ in the fluid, we used

$$j^{\rm conv}(t)=j_0^{\rm conv}(t)-j_0^{\rm conv,g}(t)\ , \tag{3.7}$$

where $j_0^{\rm conv,g}(t)$ was measured in the gel during equivalent experimental runs and where $j_0^{\rm conv}$ was determined from Eq. (3.6).

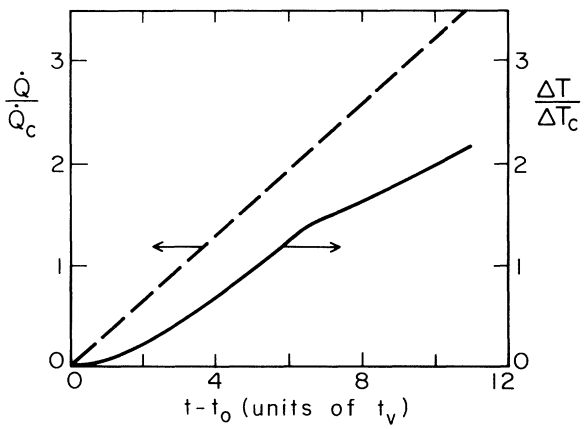

FIG. 6. Example of a ramping experiment with $\dot{Q}/\dot{Q}_c=\beta'(t-t_0)$, where $t-t_0$ is the time elapsed from the beginning of the experiment and is given in units of the vertical thermal diffusion time t_v. The variable t_0 is defined such that the temperature difference ΔT reaches its critical value ΔT_c at $t=0$. The ramp rate of the heat current is $\beta'=0.32$. The dashed curve represents the power $\dot{Q}$ applied to the bottom plate divided by its critical value $\dot{Q}_c$. The solid curve represents $\Delta T/\Delta T_c$.

IV. THEORETICAL DETERMINATION OF THE CONVECTIVE HEAT CURRENT

We wish to estimate the strength of a noise source or of a deterministic field which is required to produce the dynamics of the convective onset which we observed in the heat-current measurements. The noise strength required to explain the measurements could in principle be obtained by calculating the convected heat current from the Oberbeck-Boussinesq (OB) equations [21,22,43,44] with appropriate Langevin noise terms [50], and by adjusting the noise intensity so as to achieve a best fit to the experimental data. Because of the practical difficulties involved in this procedure, we instead compared the experimental results with two models which were derived [17,18,25,26,51,52] from the OB equations. A deterministic version of one of these models was used as well to see whether the current could be explained adequately without invoking stochastic effects.

A. Stochastic Swift-Hohenberg model

The first model used by us is the stochastic Swift-Hohenberg (SSH) model [17,26]

$$\tau_0\dot{\psi}=[\epsilon(t)-\tilde{\xi}_0^4(\nabla^2+k_c^2)^2-g_3\psi^2-g_5\psi^4]\psi+f(x,y,t)\ , \tag{4.1a}$$

with ψ a function of x, y, and t, with

$$\langle f(x,y,t)f(x',y',t')\rangle=2\tau_0\tilde{\xi}_0^2F_{\rm expt}\delta(x-x')\delta(y-y')\delta(t-t')\ , \tag{4.1b}$$

and with

$$\tilde{\xi}_0^4=\xi_0^2/(4k_c^2)\ . \tag{4.1c}$$

Sufficiently near threshold, Eq. (4.1) is equivalent to the Oberbeck-Boussinesq equations with appropriate Langevin noise terms [17,26]. With the parameters used by us, it takes into account rigid-rigid boundary conditions at the top and bottom of the cell. In order to obtain the convected current $j^{\rm conv}$, or the Nusselt number, from this model, it is necessary to first integrate this stochastic partial differential equation with two spatial dimensions to

obtain the real field ψ. The spatial average of ψ^2 is then equal to $j^{\rm conv}$. An approximate solution to this problem has been given by Hohenberg *et al.* [26]. We used this solution with our experimental values for $\epsilon(t)$ as input, and fitted the resulting $j^{\rm conv}$ to the experimental data for the convected heat current. The precise formulas employed in this analysis are given in Ref. [26].

Equation (4.1) contains several parameters. For $\sigma=6.0$ and a laterally infinite system, we expect $\tau_0=0.0552$. $\xi_0=0.3848$, $k_c=3.116$, and $g_3=0.466$ [18,22,41,47]. The coefficient g_5 of the quintic term, to our knowledge, has not been derived from theory. For the finite system, τ_0 is known to remain almost unchanged [47,53]. We have assumed that ξ_0 and k_c are also unaffected by the finite system size. Indeed, the value of k_c is in excellent agreement with the wave vectors determined in our experimental cell (see Sec. V) and shown in Fig. 22(a) below. The nonlinear parameter g_3 is increased significantly [42,46–49] relative to the infinite case, and we thus took it from independent experimental measurements under steady heating which were analyzed by fitting to a single-mode model as described below. We found that, in order to obtain agreement over a substantial range of ϵ between our static data and the single-mode model, the quintic term had to be included. It was therefore also included in Eq. (4.1).

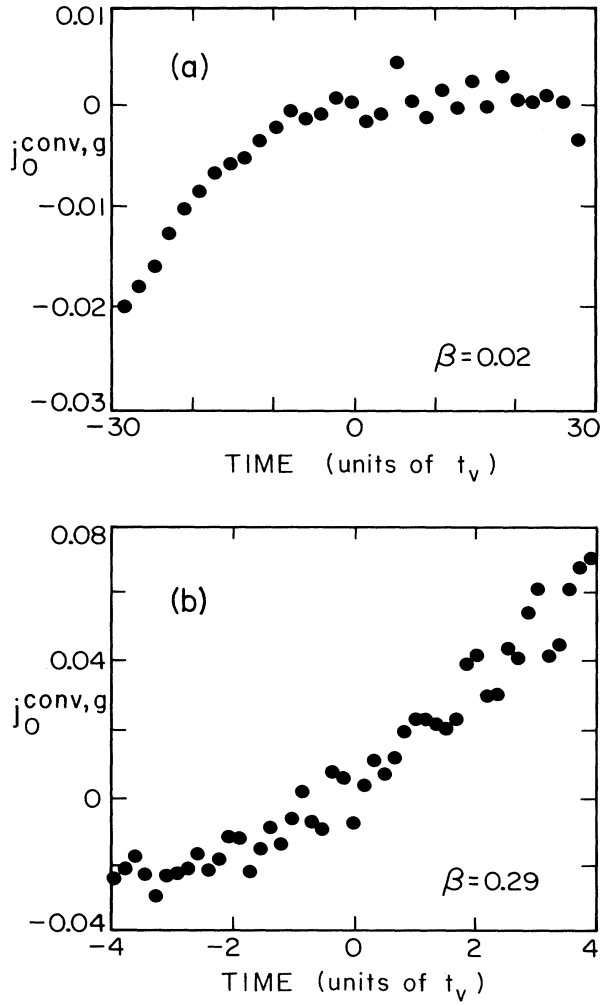

FIG. 7. Test of the accuracy of Eq. (3.6) for describing the convective heat current $j^{\rm conv}$ as a function of time. The current is in units of the heat flux at the onset of convection when the cell contains water. However, for this experiment the cell contained a gel in order to prevent convection; hence, the measured current $j_0^{\rm conv,g}$ should be zero at all times. Deviations from zero are due to initial transients with lifetimes $\approx 20t_v$. Ramp rates of the reduced Rayleigh number $\epsilon \equiv \Delta T/\Delta T_c - 1$ are (a) 0.02, (b) 0.29.

The only remaining parameter in Eq. (4.1) that needs to be determined from the dynamic experiments is the noise strength $F_{\rm expt}$. If the noise were purely of thermal origin, then this strength would be given by [26]

$$F_{\rm expt}=F_{\rm th}=\frac{k_B T}{\rho d \nu^2}\frac{0.186\sigma^2}{\sigma+0.512} . \tag{4.2a}$$

Here, k_B is Boltzmann's constant and T is the average temperature of the fluid. For our fluid we have

$$F_{\rm th}=1.71\times 10^{-9} . \tag{4.2b}$$

B. One-mode model

Rather than solving the full SSH model, integrating over space, and fitting to the experiment, it would be much simpler to solve an ordinary differential equation for $j^{\rm conv}$ directly. An approximate reduction to such an effective single-mode description of the problem has been discussed by various authors [18,25,51,52]. The one-mode model has the advantage that a direct numerical integration of the stochastic equation is feasible. Thus, the approximations here are in the derivation of the model rather than in the integration, whereas in the SSH model, it is believed that there is an exact correspondence for small ϵ between the model and the OB equations, but the solution of the model has to be obtained by approximate methods. The one-mode model also lends itself to calculating statistical properties such as the probability distribution functions in addition to the mean current [25]. We have used it as well in the analysis of the data in order to see if the two procedures reveal any significant differences due to the different approximations. We also used it as a deterministic model, with the Langevin force replaced by a constant.

We integrated numerically the equation

$$\tau_0\frac{dA(t)}{dt}=\epsilon(t)A(t)-\bar{g}_3A(t)^3-\bar{g}_5A(t)^5+\bar{f} , \tag{4.3a}$$

with [18] $\bar{g}_3=3g_3/2$, $\bar{g}_5=5g_5/4$, and took $\bar{f}$ to be either a Gaussian random force [54,55] with correlations given by

$$\langle \bar{f}(t)\bar{f}(t')\rangle = 2\tau_0\bar{F}_{\rm expt}\delta(t-t') \tag{4.3b}$$

or as a deterministic field $\bar{f}=f_{\rm Det}$. As in the SSH model, we used the experimental $\epsilon(t)$ as input. We will henceforth refer to Eq. (4.3) as the amplitude equation since it is an equation for the amplitude $A(t)$ of the field rather

than for the complete spatial variation.

We chose $\bar{g}_3$ and $\bar{g}_5$ so that

$$j^{\text{conv}} = A^2 \ . \tag{4.4}$$

Under steady heating, the left-hand side of Eq. (4.3) is zero, and for $\bar{f}=0$ the solution to the equation is Eq. (2.8). We fit measurements of j^{conv} under steady heating to Eq. (2.8) to obtain $\bar{g}_3$ and $\bar{g}_5$ (in the steady experiments, the effect of the field is negligible). For the cell with polyethylene sidewalls we obtained $\bar{g}_3 = 0.832$ and $\bar{g}_5 = -0.104$.

When $\bar{f} = f_{\text{Det}}$ was used as a deterministic field, we obtain values of j^{conv} by numerically integrating Eq. (4.3) and using f_{Det} as an adjustable parameter [18] in a least-squares fit to the data. The equation was integrated starting at the time t_0 when the experiment began, and the initial value of the amplitude was

$$A = -f_{\text{Det}}/\bar{\epsilon}_0 \ , \tag{4.5}$$

where $\bar{\epsilon}_0$ was the value of ϵ at $t = t_0$ (usually -1.0; see Sec. III A).

In the stochastic case, we set $j^{\text{conv}}(t)$ equal to $\langle A^2 \rangle$, where $\langle A^2 \rangle$ is the average of the values of A^2 obtained for a large number M of integrations of the stochastic equation (4.3), each integration being done with a different realization of $\bar{f}(t)$ [55]. Typically we used $M = 10^4$. The value of $\bar{F}_{\text{expt}}$ in Eq. (4.3b) was least-squares adjusted to provide the best agreement between experiment and theory.

In an ideal ramping experiment, the only source of stochastic perturbations would be thermal noise, yielding $\bar{F}_{\text{expt}} = \bar{F}_{\text{th}}$ in the model. For a system with free-free boundary conditions and a single unstable mode, $\bar{F}_{\text{th}}$ was derived in Ref. [18]. Van Beijeren and Cohen [51,52] have made calculations of $\bar{F}_{\text{th}}$ for a system with the more realistic rigid-rigid boundary conditions and with an ϵ-dependent band of unstable modes. For a ramping experiment, they obtained

$$\bar{F}_{\text{th}} = \left[\frac{1}{2\pi\tau_0 t} \right]^{1/2} \left[\frac{k_B T t_v k_c^2}{2.42 \rho d^3 \nu R_c} \right] \ . \tag{4.6a}$$

Note that the *effective* noise strength $\bar{F}_{\text{th}}$ varies slowly with time. For our parameters and with $t = 2$ (a typical onset time), Eq. (4.6a) yields

$$\bar{F}_{\text{th}} = 2.8 \times 10^{-11} \ . \tag{4.6b}$$

It is useful to illustrate the experimentally observed dynamics in terms of the dynamics of Eq. (4.3) with $\bar{f} = f_{\text{Det}}$. If $A = 0$ is an initial state of the system, then Eq. (4.3) with $\bar{f} = 0$ predicts that the amplitude will never change to a nonzero value, even when $\epsilon > 0$. The fact that convection does evolve in the physical system for $\epsilon > 0$ is incorporated in Eq. (4.3) by adding the forcing field $\bar{f}$. In ramping experiments, the strength of the field $\bar{f}$ determines the time delay after $\epsilon = 0$ is passed before convection reaches a macroscopic amplitude. This is illustrated in Fig. 8, which shows A^2 as a function of time, where the values of $\epsilon(t)$ were taken from a ramping experiment with $\beta = 0.29$. The dashed curve represents the quasistatic values $j_{\text{qs}}^{\text{conv}}$ obtained for $\bar{f} = 0$ from Eq. (2.8). The solid curves result from numerically integrating Eq. (4.3) with constant deterministic fields of (a) $\bar{f} = f_{\text{Det}} = 10^{-2}$, (b) 10^{-4}, and (c) 10^{-6}. Once the convective amplitude reaches a macroscopic value, it grows rapidly until it almost reaches its quasistatic value, as is shown by solid curves (b) and (c). [The solid curve (a) appears to actually reach the quasistatic value but this does not occur; a field of $\bar{f} = 10^{-2}$ is large enough to

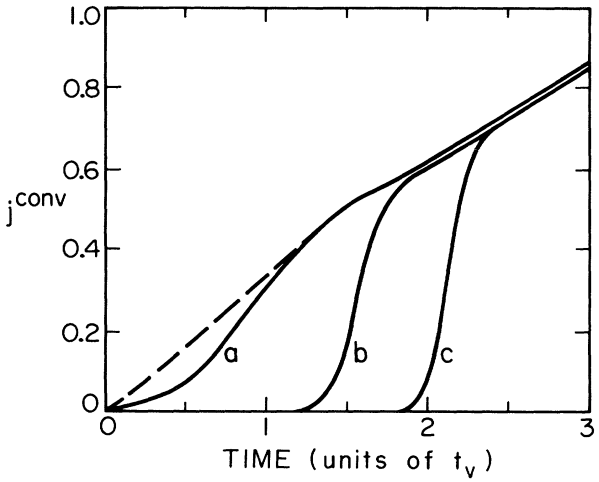

FIG. 8. Predictions of the amplitude equation with an adjustable deterministic field f [Eq. (4.3a)] for the convective heat current $j^{\text{conv}}(t)$ during a ramping experiment with ramp rate $\beta = 0.29$ (shown as the solid curves). The field values represented are (a) $f = 10^{-2}$, (b) 10^{-4}, and (c) 10^{-6}. The value of f corresponding to the experiment can be determined by adjusting f so as the provide the best fit to the data. The dashed curve represents the quasistatic value of j^{conv} (see text).

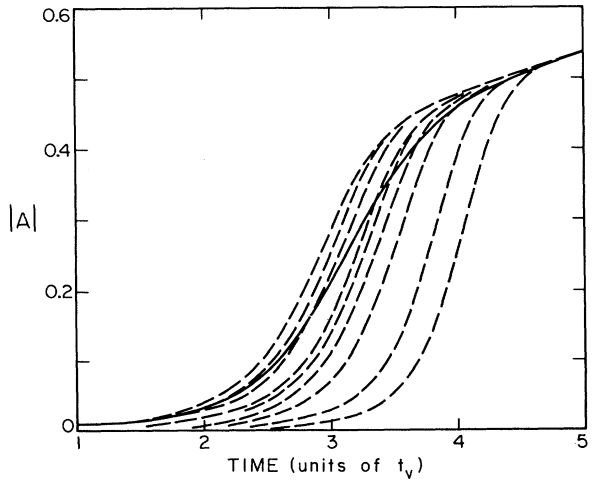

FIG. 9. Several integrations of the stochastic amplitude equation [Eq. (4.3)], each with a different realization of the stochastic field $\bar{f}(t)$ of intensity $\bar{F} = 5 \times 10^{-7}$, are shown as dashed lines for a ramp rate $\beta = 0.05$. The solid line is the average of 10^4 such integrations.

significantly increase $j_{qs}^{conv}(\epsilon)$ above the values shown by the dashed curve in the figure.] As can be seen from the figure, extremely small values of $\bar{f}$, the effect of which would not be observable in static experiments, are sufficient to cause the convective onset at relatively short times.

We note that the deterministic and stochastic versions of the amplitude equation give quite different results for the shape of $j^{conv}(t)=\langle A^2\rangle(t)$. The stochastic model gives a current which rises more slowly, i.e., with a smaller slope, than the deterministic model. This difference is attributable to the averaging over many realizations of $A^2(t)$. Any one realization has a shape very similar to the deterministic case; but the probability distribution $P(A)$ is such that $\langle A^2\rangle(t)$ increases more slowly with time. This is illustrated in Fig. 9, where we show a small number of stochastic integrations as dashed lines, as well as the average of 10^4 integrations as a solid line, for a ramp rate $\beta=0.05$ and for $\bar{F}=5\times10^{-7}$. It is apparent that one should be able to distinguish between a stochastic and a deterministic process by examining the shape of j^{conv}.

V. RESULTS

A. Deterministic onset with a high-density polyethylene sidewall

We first performed the ramping experiments using a high-density polyethylene (HDPE) sidewall of the geometry shown in Fig. 1. An example of patterns observed and heat fluxes measured with a ramp rate $\beta=0.27$ is shown in Fig. 10. The experimental convective heat current, obtained as described in Sec. III B, is plotted as open circles in the bottom of the figure. The convection did not achieve a macroscopic amplitude until over one vertical diffusion time had elapsed since the convective threshold had been passed. Once it started to grow, however, it rose rapidly toward (but, of course, never quite reached) its quasistatic value.

The heat-flux prediction of the amplitude equation with the best-fit deterministic field $f_{Det}=2.8\times10^{-4}$ is shown in the plot of Fig. 10 as the solid curve. The agreement with the experimental points is very good. The dashed curve shows the solution of the amplitude equation with a stochastic field that has a best-fit noise strength [27–29,56] of $\bar{F}_{expt}=2.6\times10^{-6}$. A fit of the SSH model to the data is indistinguishable from the dashed line, and yields $F_{expt}=1.1\times10^{-4}$. The dashed curve also agrees well with the measurements. Thus, as in earlier work [18], it is impossible to determine reliably from these heat-flux measurements whether the perturbations causing the onset of convection are deterministic or stochastic in their origin.

In the top portion of Fig. 10 are four images that were taken during the run at the time when the convection pattern was emerging. The solid circles in the plot underneath show the heat-flux points that were measured at the time the images were made. The pattern clearly reflects the geometry of the sidewall. The circular rolls at first are strongest adjacent to the sidewall, and then evolve towards a state of uniform amplitude. With this sidewall, we found the circular rolls to be reproducible from one experimental run to the next. The circular pattern is in agreement with earlier experiments [57–60] on pattern formation in Rayleigh-Bénard convection and confirms that in this type of cell the pattern-formation process is dominated by deterministic forcing from the sidewall.

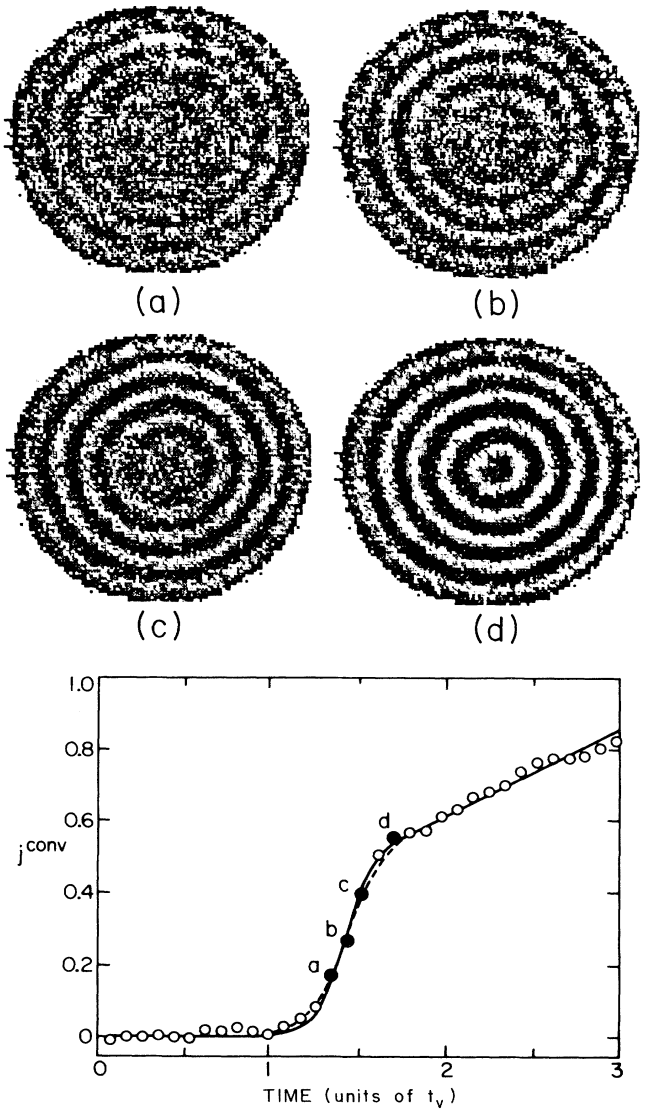

FIG. 10. Shadowgraph images (unfiltered) of the emerging pattern, and data for the convective heat flux j^{conv}, as a function of time, resulting from a ramping experiment with ramp rate $\beta=0.27$, for a cell with a high-density polyethylene sidewall and a sapphire top. Solid circles correspond to the points where the images were taken. The solid curve represents the prediction of the amplitude equation with a best-fit deterministic field $f_{Det}=2.8\times10^{-4}$, and the dashed curve represents the prediction of the amplitude equation with a stochastic field with a best-fit noise intensity $\bar{F}_{expt}=2.6\times10^{-6}$ or the SSH model with a best-fit noise intensity of $F_{expt}=1.1\times10^{-4}$.

Experimental runs were done for a number of other ramp rates. We found that as the ramp rate was decreased, the onset time for convection increased, in agreement with previous observations [18]. For $0.08 \leq \beta < 0.30$, the agreement between the theoretical and experimental values of j^{conv} was as good as that shown in Fig. 10. For $\beta < 0.08$, however, the agreement progressively worsened. The measured convective heat current, once it became macroscopic, did not grow as fast as the amplitude equation predicted. During all the runs, however, the convective pattern emerging was identical to that shown in Fig. 10. We believe that the problems at small ramp rates are caused by insufficiently accurate modeling of thermal effects (see Sec. III B) due to the finite conductivity of the sapphire plate. This is supported by the fact that a similar difference between the prediction and the data for runs with a gel sidewall (see Sec. V B below) was essentially eliminated by replacing the sapphire with a copper plate, as will be described.

In Fig. 11 the open circles are the best-fit values [61] of the deterministic field f_{Det} as a function of ramp rate (the open squares and solid circles correspond to runs with a gel wall and will be discussed in the Sec. V B). The values of f_{Det} are all of order 10^{-4}, and they increase monotonically with β. These results are similar to those reported by ACHS [18] for liquid helium with a thin stainless-steel sidewall. The results of ACHS are shown as a dashed line in Fig. 11 [62].

The pattern-formation process described above has been discussed theoretically by ACHS [18] and considered quantitatively by Cross *et al.* [24]. The forcing of a roll pattern parallel to the sidewall occurs due to a mismatch between the thermal diffusivity of the fluid and the wall. Upon time-dependent heating, the fluid and wall warm up at different rates, resulting in lateral temperature gradients in the fluid adjacent to the wall. Conduction is unstable to convection for any finite, lateral temperature gradient [63] so in ramping experiments a weak roll pattern begins next to the wall before ϵ becomes positive. As ϵ increases, the pattern gradually fills the entire cell. An expression has been derived [Eq. (38) of Ref. [24]] for the deterministic field in the amplitude equation which accounts for the thermal forcing of rolls by the sidewall. For the mismatch between the HDPE sidewall ($\Lambda = 4.9 \times 10^{-3}$ W/cm K, $\kappa = 2.2 \times 10^{-3}$ cm^2/sec) [64] and water (whose properties are listed in Sec. II A), it yields [65] $f_{\text{Det}} = f_1 \beta$, where $f_1 = 1.9 \times 10^{-3}$. Although the increase of f_{Det} in Fig. 11 is not linear over the whole range of β, we have drawn a straight solid line through the points with $\beta < 0.1$ to compare with the theoretical prediction. This line has a slope of $f_1 = 1.7 \times 10^{-3}$ and a y intercept of $f_0 = 5 \times 10^{-5}$. The value of f_1 is in remarkably good agreement with the prediction. A nonzero value of the static field f_0, however, is not accounted for by the work of Ref. [24]. As can be seen from the dashed line in Fig. 11, a static field of similar size has been observed also by ACHS [18]. It was attributed by them to small geometrical imperfections in their cell [66,67]. Our present cell has a much more nearly perfect geometry than that of ACHS, and we believe that this source of imperfection is greatly reduced. However, a further source of a static field which has recently become appreciated is static thermal sidewall forcing. This forcing results from lateral temperature gradients in the fluid adjacent to the sidewall caused by a mismatch between the thermal conductivities of fluid and sidewall combined with the finite thermal conductivity of the top and/or bottom plates [23,63]. However, this thermal forcing should be largely eliminated by the sidewalls described in Sec. V B.

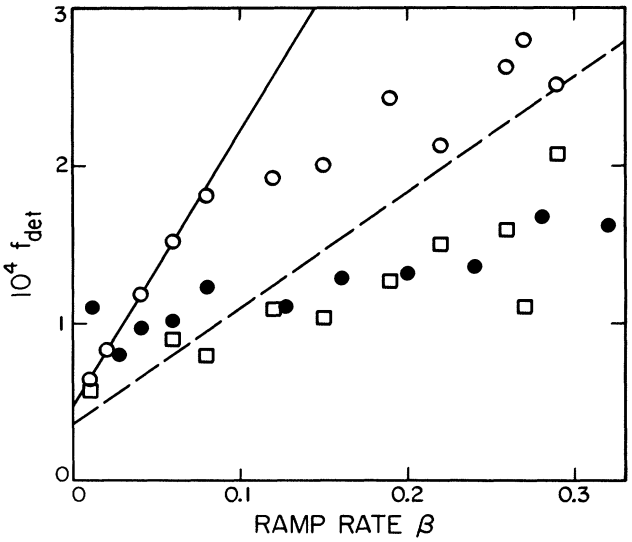

FIG. 11. Experimental best-fit values of the deterministic field f_{Det} of the amplitude equation as a function of the ramp rate β. The open circles were obtained with the high-density polyethylene sidewalls. The open squares are for the gel sidewall and the sapphire top, and the solid circles are for the gel sidewall and the copper top. The solid line through the open circles for $\beta < 0.1$ is described by $f_{\text{Det}} = f_0 + f_1 \beta$, where $f_0 = 5 \times 10^{-5}$ and $f_1 = 1.7 \times 10^{-3}$. The dashed line corresponds to the field values obtained in an earlier experiment [18].

From the patterns in Fig. 10, as well as from the good agreement between the theoretical and experimental values of f_1, we conclude that the convective onset is dominated by deterministic effects when the fluid is water and the sidewalls are made of HDPE.

B. Stochastic onset with a gel sidewall

While the sidewall-induced perturbations which force circular roll patterns are of interest, they mask the perturbations that would otherwise determine the pattern-formation process. These smaller perturbations would presumably dominate in a horizontal laterally infinite system where there are no walls, provided the thickness and the heating are uniform. In order to observe them, we used sidewalls that have thermal properties sufficiently close to those of water. Unfortunately, the materials usually used do not fulfill this criterion. We tried using a number of different plastics, but forcing of concentric roll patterns occurred with all of them. We solved this problem by using a sidewall with an inner annulus composed of a gel of 95% water and 5% polyacrylamide. The

thermal properties of such a gel are virtually the same as those of water. We washed the gel in circulating water for two weeks after preparation to avoid contaminating the water in our cell. The inner and outer radii of the gel differed by $1.75d$ and it had a height that was between $0.8d$ and $1.0d$. It was sufficiently rigid to maintain its original shape under the force of gravity. The aspect ratio of the fluid was the same as that of the previous sidewall ($L=10$). Outside the gel annulus, the sidewall was identical to the previous one.

In Fig. 12 we show patterns and heat-flux measurements obtained with the gel sidewall. The ramp rate was the same as that used in Fig. 10 ($\beta=0.27$). As before, the circles in the plot represent experimental measurements,

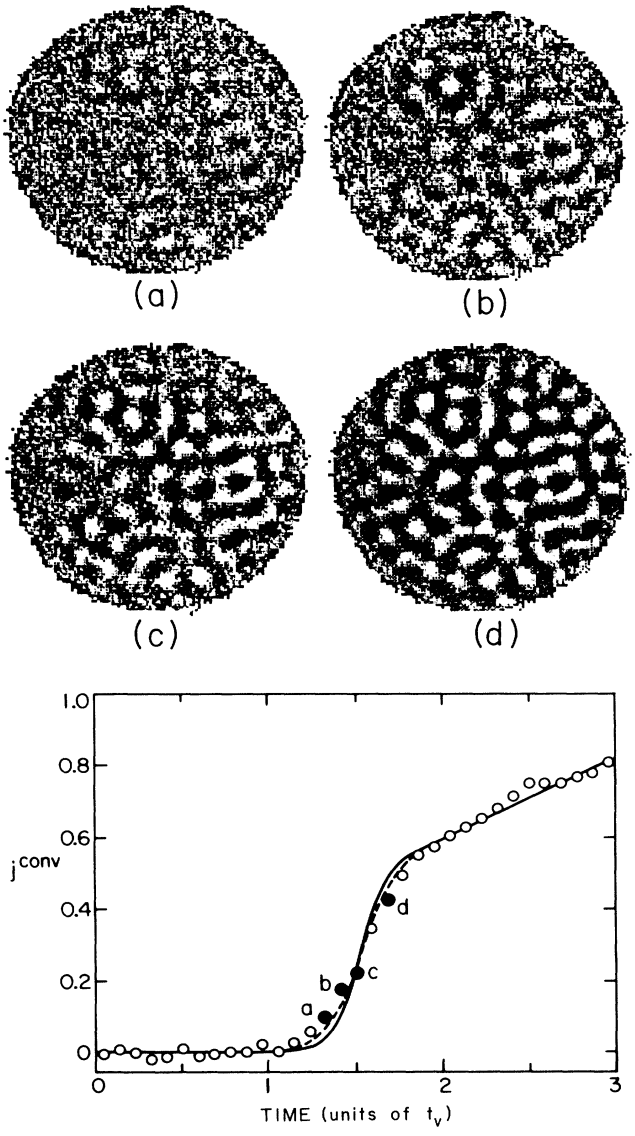

FIG. 12. Images (unfiltered) and convective-heat-flux data as in Fig. 10 for the same ramp rate, but for a cell with a sidewall made of 5% polyacrylamide gel. The best-fit value of the deterministic field is $f_{\mathrm{Det}}=1.1\times10^{-4}$, and that of the stochastic noise intensity is $\bar{F}_{\mathrm{expt}}=5.3\times10^{-7}$ and $F_{\mathrm{expt}}=2.4\times10^{-5}$.

and the solid (dashed) curve shows predictions of the amplitude equation with a best-fit deterministic (stochastic) field. The best-fit value of the deterministic field is $f_{\mathrm{Det}}=1.1\times10^{-4}$ and that of the noise intensity of the stochastic field for the amplitude equation is $\bar{F}_{\mathrm{expt}}=5.3\times10^{-7}$. As for the case of Fig. 10, a fit of the SSH model to the data is indistinguishable from the dashed line. Such a fit yielded $F_{\mathrm{expt}}=2.4\times10^{-5}$. These are smaller values than were obtained with the HDPE wall, but the value of $\bar{F}_{\mathrm{expt}}$, for instance, is still much larger than $\bar{F}_{\mathrm{th}}$ given in Sec. IV A. It is remarkable that, despite the considerably better match in thermal properties between the fluid and sidewall, j^{conv} increases noticeably above zero only $\approx0.1t_v$ later than for the case of Fig. 10. This increased onset time for convection results in a decrease in the best-fit value of f_{Det} by approximately a factor of 2.

The stochastic models fit the data in Fig. 12 somewhat better than the deterministic model. However, more convincing evidence for the stochastic nature of the convective onset in the presence of a gel sidewall comes from the nature of the evolving flow field. The images of Fig. 12 show the emergence of the convective pattern for $\beta=0.27$. The pattern observed is dramatically different from that of Fig. 10, and is typical of the patterns which emerged during all ramping experiments performed with the gel wall. It is no longer composed of rolls, but rather of a set of irregularly arranged cells with no clear geometrical structure. Although the pattern emerges in various places throughout the container, it appears first in a small patch in the upper portion of the image. The exact location of the initial pattern emergence is not reproducible from one experimental run to the next. The locations of the cells do not reflect the container geometry, implying that the perturbations determining this pattern are not generated by the sidewall.

Figure 13 shows the results for the very small ramp rate $\beta=0.01$. Here, the best-fit deterministic field is $f_{\mathrm{Det}}=6\times10^{-5}$, and the best-fit stochastic-field noise strength for the amplitude equation is $\bar{F}_{\mathrm{expt}}=6\times10^{-7}$. The agreement between experiment and theory is not nearly as good as at higher ramp rates. Results with $\beta=0.01$ obtained while using the HDPE sidewall are similar. As with the HDPE sidewall, the agreement is very good for $0.08\leq\beta\leq0.30$, but becomes progressively poorer as β is decreased below 0.08. The images of Fig. 13, however, show that the pattern still emerges with a random cellular structure.

The poor correspondence at the small ramp rates between the models and the measured currents was largely eliminated by replacing the sapphire top with the top laminated from copper and acrylic (in that case, of course, no images of the flow field could be obtained). We believe that the difference between the models and the data taken with the sapphire top is attributable to errors in our estimate of j^{conv} associated with the fact that the temperature difference across the sapphire plate and the boundary layer was included in ΔT. With the laminated top, we used a thermistor embedded directly in the copper to determine the temperature of the top plate. Because of the high thermal conductivity of copper, this

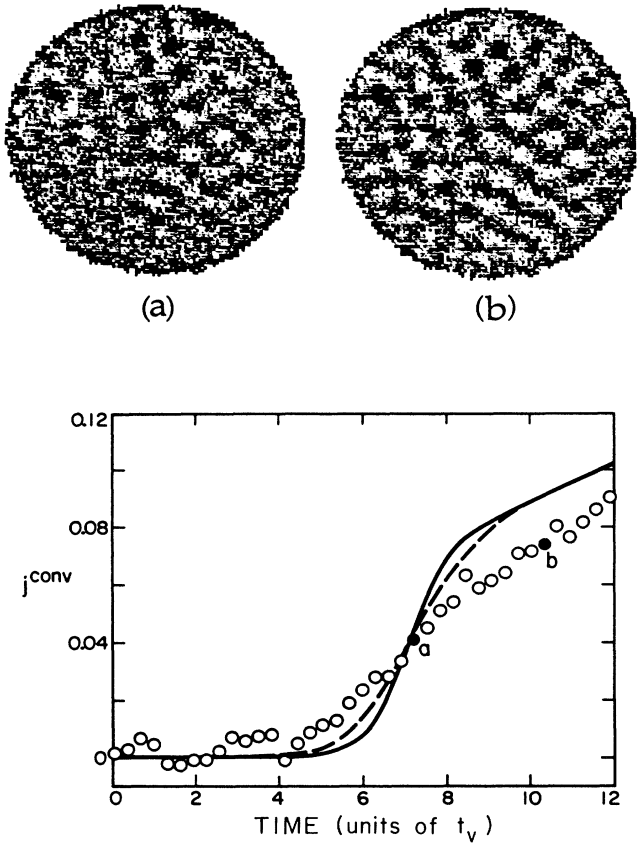

FIG. 13. Images (unfiltered) and convective-heat-flux data as in Fig. 12 but with a ramp rate of 0.01. The best-fit value of the deterministic field is $f_{Det}=6\times10^{-5}$, and the intensity of the best-fit stochastic field is $\bar{F}_{expt}=6\times10^{-7}$.

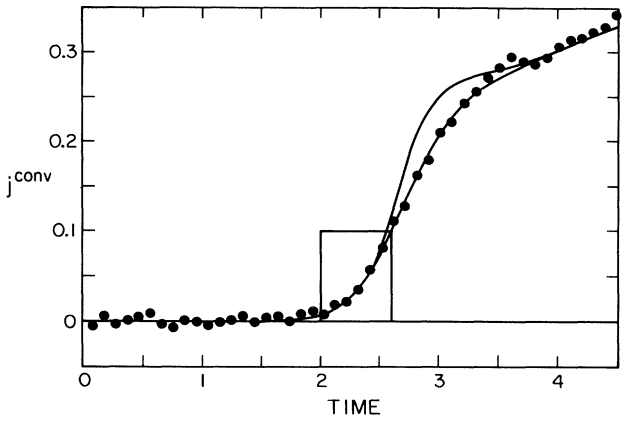

FIG. 14. Data for the convective heat flux j^{conv}, as a function of time, resulting from a ramping experiment with ramp rate $\beta=0.08$, for a cell with a gel sidewall and a copper top. The upper curve represents the prediction of the amplitude equation with a best-fit deterministic field $f_{expt}=1.2\times10^{-4}$. The lower curve is the prediction of the amplitude equation with a stochastic field intensity of $\bar{F}_{expt}=0.6\times10^{-6}$ or the SSH model with a stochastic field intensity of $F_{expt}=3.4\times10^{-5}$. All fits were obtained using only the data in the small rectangle where the current first becomes macroscopic.

temperature was very uniform even at the critical heat current, and virtually equal to the temperature at the top of the fluid. Thus, the measured and actual values of ΔT were almost exactly equal. For $\beta=0.08$ the measured heat current with the copper top is shown in Fig. 14. Here the upper and lower solid lines are the fit to the amplitude equation with the deterministic and stochastic field, respectively. The stochastic model fits the data well at this smaller ramp rate, but the deterministic model does not provide a very good fit. The fields are $f_{Det}=1.2\times10^{-4}$, $\bar{F}_{expt}=0.6\times10^{-6}$, and $F_{expt}=3.4\times10^{-5}$. Similar results for $\beta=0.01$ are given in Fig. 15. Even at this very small ramp rate, the stochastic model (lower curve) fits well; however, the deterministic model (upper curve) provides only a poor fit. For this case the parameters are $f_{Det}=1.2\times10^{-4}$, $\bar{F}_{expt}=1.5\times10^{-6}$, and $F_{expt}=9\times10^{-5}$. At these small ramp rates the difference in the quality of the fit between the deterministic and stochastic models provides convincing evidence in favor of the latter.

Figures 16(a) and 16(b) display best-fit field-intensity values for the stochastic amplitude equation and for the SSH model, respectively, as a function of ramp rate. The solid circles are for the gel sidewall and the copper-laminate top, and the open squares are for the gel wall and the sapphire top. The results of fitting the deterministic amplitude equation to the data for the gel sidewall were shown in Fig. 11, again using solid circles and open squares for the copper and sapphire tops, respectively. We carried out these deterministic fits even though we believe that a deterministic model is inappropriate in these cases so as to facilitate a comparison

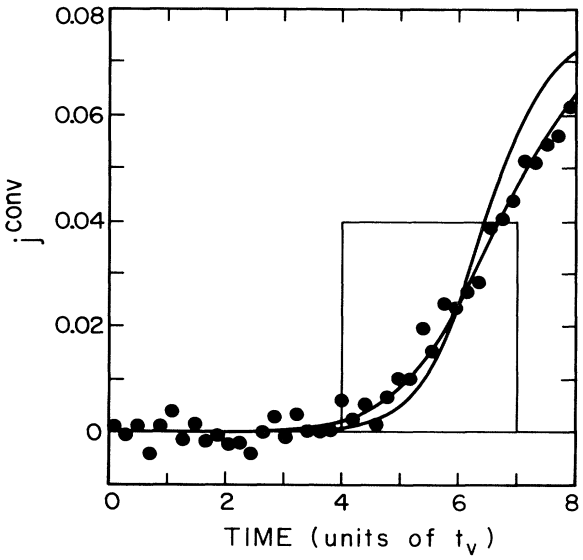

FIG. 15. Data for the convective heat flux as in Fig. 14, but for $\beta=0.01$. The steeper curve corresponds to $f_{expt}=1.2\times10^{-4}$, and the other curve is for $\bar{F}_{expt}=1.5\times10^{-6}$ and for $F_{expt}=9\times10^{-5}$.

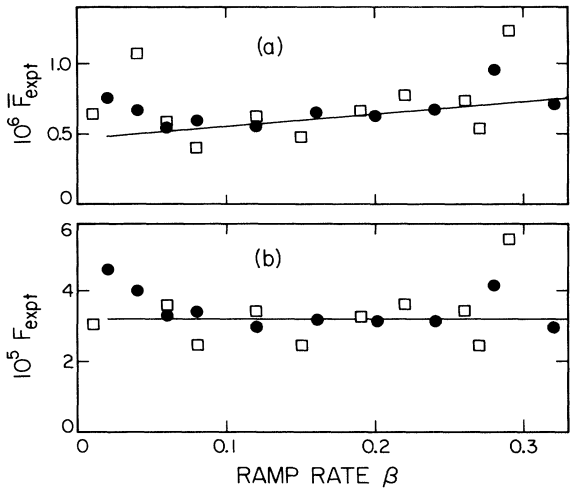

FIG. 16. Best-fit field-intensity values for experiments performed with a gel sidewall. The open squares are for the measurements with a sapphire top, and the solid circles are for the runs with the copper-laminate top. The top figure (16a) gives the results for $\bar{F}_{expt}$ obtained from fits to the stochastic amplitude equation. The bottom figure (16b) gives values of F_{expt} obtained by fitting the same experimental data to the stochastic Swift-Hohenberg model.

between the cells with different sidewalls.

The deterministic field-intensity values for the gel wall in Fig. 11 (open squares and solid circles) are within experimental scatter independent of the nature of the top plate. A straight line drawn through them has a slope $f_1 = 2.7 \times 10^{-4}$ and a y intercept of $f_0 = 8 \times 10^{-5}$. The value of f_0 is similar to the one for the HDPE walls, even though the patterns consist of random cells in the former case, and of concentric rolls in the latter. We do not have a good explanation of the results for f_0. The value of f_1 is much smaller for the gel walls than for the HDPE walls, showing that the dynamic sidewall forcing has been significantly reduced or eliminated. A quantitative interpretation of f_1 for the gel walls should not be attempted, however, because the deterministic sidewall-forcing model of Cross *et al.* [24] would not be expected to be applicable when the pattern which evolves does not have the symmetry of the walls.

For the SSH model, a constant field intensity is expected, independent of the ramp rate. The data in Fig. 16(b) are consistent with this for $\beta \gtrsim 0.05$, as indicated by the horizontal line in the figure. They give $F_{expt} = 3.2 \times 10^{-5}$, and thus, with Eq. (4.2b),

$$F_{expt}/F_{th} = 1.9 \times 10^4 . \quad (5.1a)$$

For the stochastic amplitude equation, the effective field intensity $\bar{F}_{expt}$ is expected [51,52] to vary as $t^{-0.5}$, where t is a "typical" time for the run. A suitable choice for t might be the time t_0 at which j^{conv} first becomes experimentally noticeable. This time changes from about 2.3 to about 1.3 as β changes from 0.08 to 0.32. The line drawn through the points in Fig. 16(a) has the corresponding β dependence. Consistent with the model, the expected slight rise in $\bar{F}_{expt}$ is more nearly consistent with the data for $\beta \gtrsim 0.05$ than a constant would be. With Eq. 4.6(b), the experimental field intensities yield

$$\bar{F}_{expt}/\bar{F}_{th} = 2.0 \times 10^4 . \quad (5.1b)$$

Thus, we see that the noise intensity required to explain the experiments is larger than the predicted thermal noise intensity by a factor of about 20 000 in both models. We have no explanation for this discrepancy.

For $\beta \lesssim 0.05$, most of the measured field intensities for both stochastic models lie somewhat above the lines through the data at higher ramp rates in Figs. 16(a) and 16(b). We have no explanation for this slight departure from the predictions of the models, but we note that the experiments become very delicate at very small β.

The irregular nature of the patterns in Figs. 12 and 13, as well as the comparison of the currents, particularly at the small ramp rates, provide considerable evidence in favor of a stochastic interpretation of the observed convective onset. Strong additional evidence comes from a lack of repeatability of the emerging patterns in nominally identical experimental runs. This is illustrated in Fig. 17, which shows images of the emerging pattern from four separate runs with the gel sidewall and $\beta = 0.27$. All images were taken at the time corresponding to image (d) in Fig. 12. The cells are located in different places in the different runs, causing no two patterns to be the same. Images taken at earlier times during these runs revealed that the spatial regions where convection first emerged differed from one run to the next. The irreproducibility

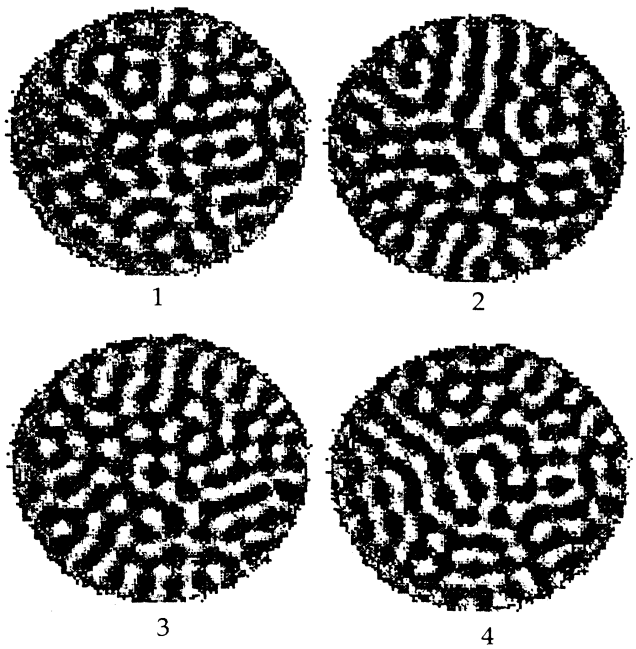

FIG. 17. Emerging patterns for consecutive experimental runs, all with ramp rate $\beta = 0.27$, for the cell with a gel sidewall. The images were taken at the time corresponding to point d in Fig. 12, and clearly show that the emerging pattern is not reproducible.

of the patterns implies that the perturbations responsible for the onset of convection in this cell are stochastic in origin, and contrasts with the reproducible results obtained with the HDPE sidewall. This suggests that when deterministic thermal sidewall forcing is sufficiently reduced, noiselike perturbations dominate the pattern-formation process.

In order to be sure that the cellular flow we observed was not geometry dependent, we also performed ramping experiments using a cell with a square sidewall. The depth of the cell was the same as before, and the aspect ratio of the cell, here defined as $L \equiv l/2d$ (where l is the length of one side of the cell), was $L = 6.5$. The inner wall was composed of a polyacrylamide gel of width $\approx 1.75d$. Shown in Fig. 18 are images of emerging patterns from four separate experimental runs with $\beta = 0.27$. The images were taken at times close to that of image (d) of Fig. 12. As with the cylindrical cell, the emerging patterns are cellular with no obvious regular structure, and do not reflect the geometry of the cell. The cells appear in different places during different runs, indicating pattern irreproducibility. We conclude that the random cellular flow observed when using the gel wall is geometry independent.

Although the cells observed in the emerging pattern had a random placement, they did have a characteristic length scale. This is illustrated in Fig. 19(a), which shows the low-wave-vector portion of the magnitude of the Fourier transform of image (d) in Fig. 12. The transform is of the entire image. The magnitude of the transform is highest near a circle, although the distribution of the magnitude around this circle is irregular. The average wave number of the pattern is measured (see Sec. II D) to be $\bar{k} = 1.01 k_c$. For comparison, we have shown in Fig. 19(b) the magnitude of the transform of image (d) in Fig. 10, which is composed of concentric rolls with $\bar{k} = 1.03 k_c$. The magnitude of this transform is also contained near a circle, although now the angular distribution around the circle is more uniform. (Note that information which further distinguishes the two patterns is held in the phase of the transform, which we have not plotted here.)

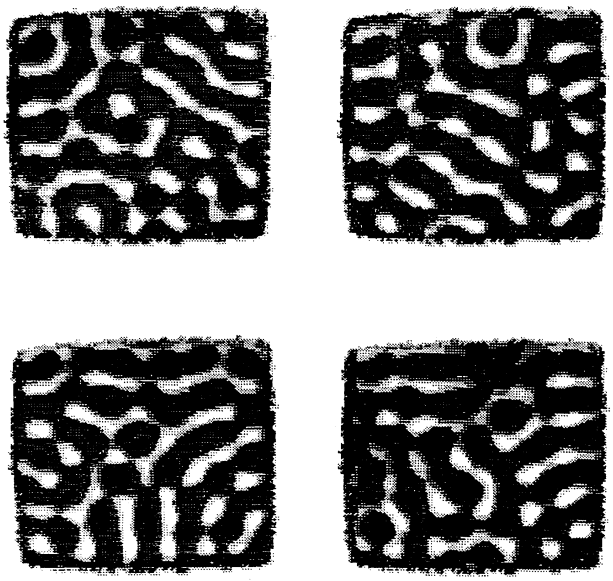

FIG. 18. Emerging patterns for consecutive experimental runs, all with ramp rate $\beta = 0.27$, for a square cell with a gel sidewall. The images were taken approximately at the time corresponding to point d in Fig. 12, and demonstrate that the irreproducible cellular patterns described in this paper are not dependent on the container geometry.

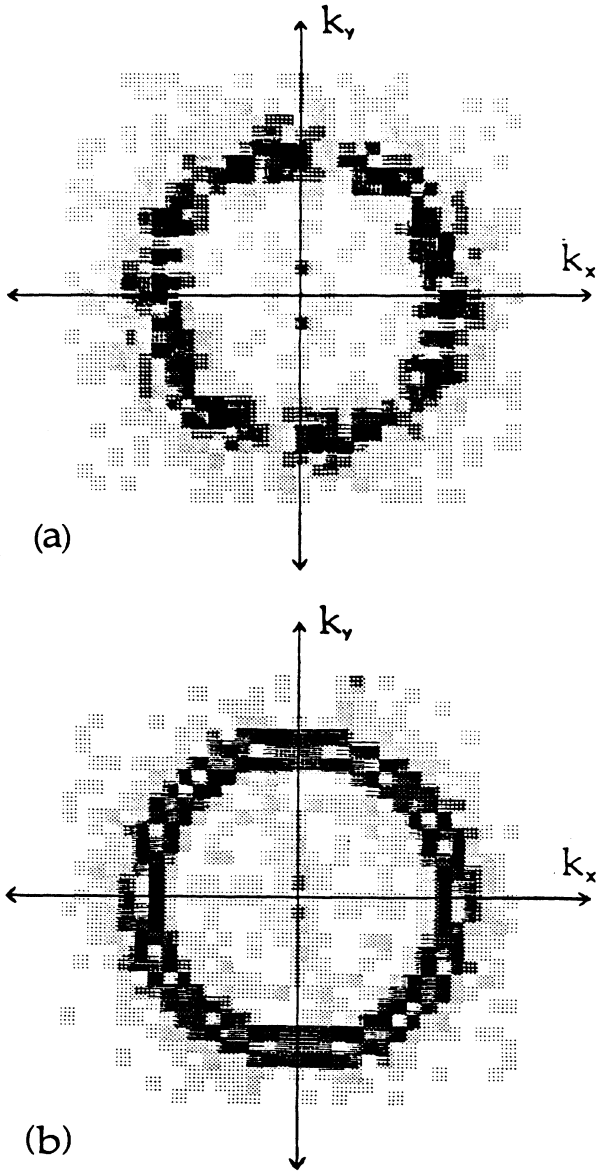

FIG. 19. Low-wave-vector portion of the Fourier transform of (a) image (d) in Fig. 12 and (b) image (d) in Fig. 10.

C. Deterministic nonlinear processes at late times

The cellular patterns which formed during the ramping experiments were not stable once they emerged. Instead, they evolved over several time units into irregular roll-like patterns. This is illustrated in Fig. 20, which shows the evolution of the pattern of Fig. 12 at later times. Below the images is a plot of the measurement of the convective heat current. In this example, the pattern takes $\approx 3t_v$ to evolve from a cellular to a roll-like structure. This healing process is similar to that found in simulations of convective pattern evolution by Greenside and Coughran [19] in which the early pattern was a random cellular flow similar to that shown in Fig. 12.

The evolution of the pattern can be better illustrated by displaying images of it with only two grey levels. Figure 21 shows the central portion of the images of Fig. 20 using this technique. The healing becomes apparent as the black and white regions connect with themselves. This healing can be quantified by measuring the total length B of the boundary between the black and white regions. A cellular pattern has a larger boundary length than a roll pattern, and therefore B should decrease during the course of the evolution. Although in a finite-size container, no two cellular (or roll-like) patterns can be expected to have exactly the same boundary length, a plot of B as a function of time for a given run is useful for illustrating the evolution. Our method for measuring B is described in the Appendix. Shown in the plot of Fig. 21

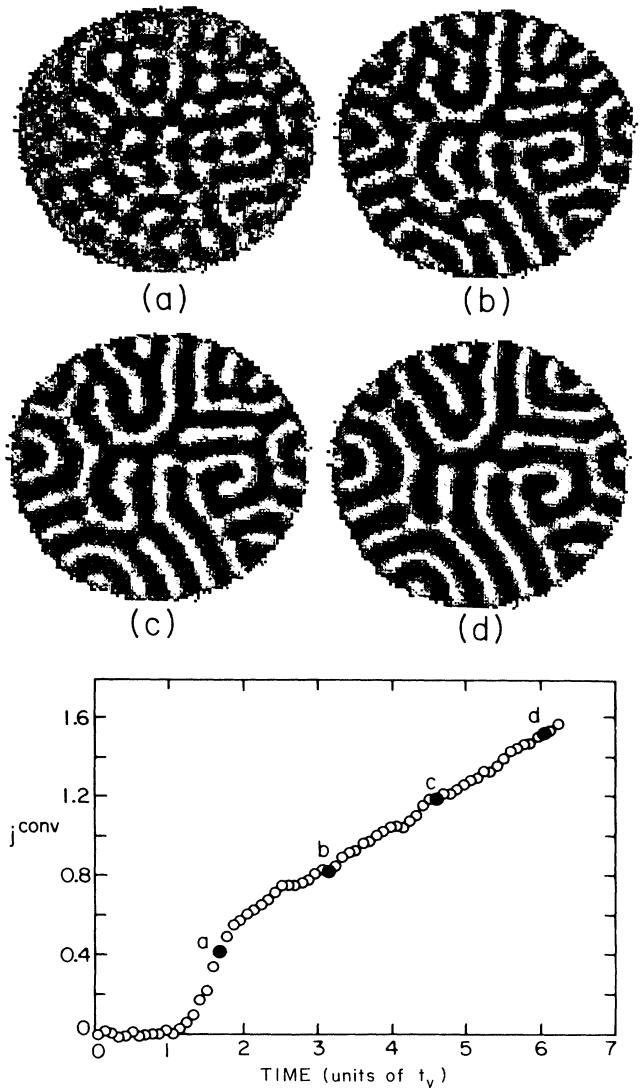

FIG. 20. Evolution of the pattern of Fig. 12, under continued ramping, showing healing leading to a roll-like structure. Heat-flux data are also shown, with point a corresponding to point d of Fig. 12.

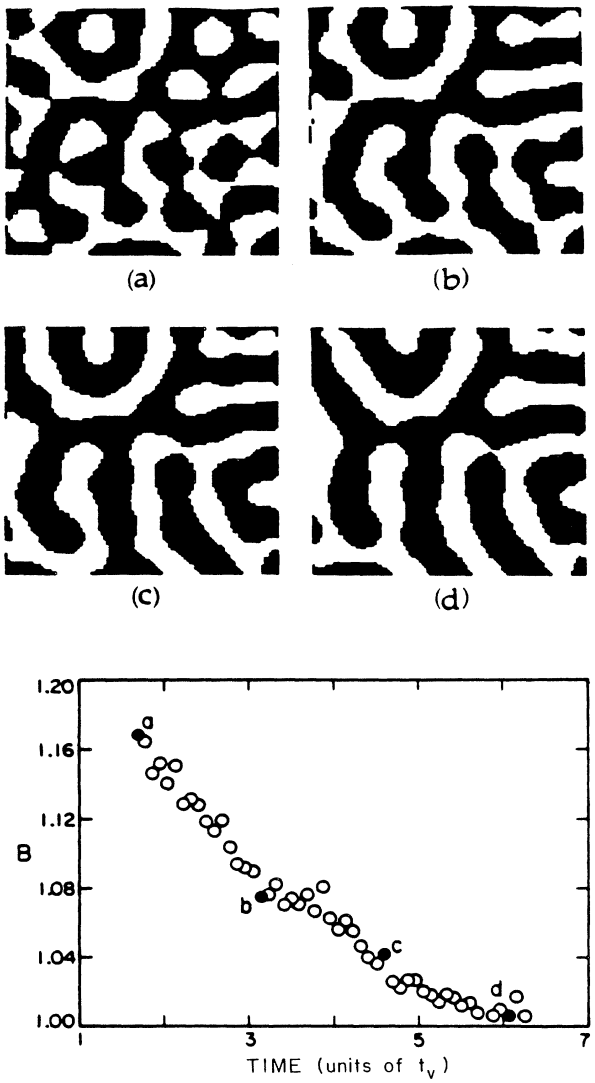

FIG. 21. Central portions of the images shown in Fig. 20, but represented with only two grey levels in order to illustrate the "connectivity" of the randomly placed cells, which develops as the pattern evolves to a roll-like structure. The plot underneath shows the total boundary length B of the image (see text) as a function of time. The solid circles correspond to the images above.

is B as a function of time. The solid circles are the points corresponding to the images shown above. The boundary length decreases monotonically so that at $t=6t_v$ its value is about 85% the value it had when the pattern first formed. Note also that the decrease is monotonic; none of the early evolutionary motions leads to even a temporary increase of the boundary length. We believe that this healing is a deterministic process associated with nonlinear effects in the finite-amplitude pattern which, in the absence of sidewalls and at large times, would lead to the parallel convection rolls predicted by Schlüter *et al.* [22].

Another characteristic of the evolution of the pattern shown in Fig. 12 is the increase of its average wavelength. This increase is illustrated in Fig. 22(a), which shows the average wave number $\bar{k}$ divided by k_c as a function of time. It monotonically decreases from $\bar{k}/k_c=1.01$ at $t=1.5$ to $\bar{k}/k_c=0.91$ at $t=6.5$. The standard deviation σ_k of k from $\bar{k}$, shown in Fig. 22(b), increases by 14% during this period of time. The decrease of $\bar{k}$ with time is consistent with results found in earlier studies [23,68–71] on wavelength selection in Rayleigh-Bénard convection, which have found that k decreases as ϵ increases. However, this earlier work involved different wave-number selection mechanisms. For comparison with these studies, we have plotted in Fig. 22(c) the relation between $\bar{k}$ and ϵ. The value to which $\bar{k}$ evolves (≈ 0.92 at $\epsilon \approx 1.2$) is in reasonable agreement with the values of $k(\epsilon)$ reported for instance, in Ref. [71] and in Ref. [23] under static conditions. Note that the evolution of $\bar{k}$ has no influence on the values of B shown in Fig. 21, since the normalization factor for B accounts for possible changes in $\bar{k}$.

It is not clear from the results presented so far whether the evolution from cellular flow to roll flow in Fig. 20 was due to the time dependence of ΔT throughout the experiment or due instead to the macroscopic amplitude of the convection. In order to clarify this matter, we performed a different ramp experiment, where we ramped up the power applied to the bottom plate such that

$$\dot{Q}/\dot{Q}_c = \begin{cases} \beta'(t-t_0)\ , & t-t_0 \le 1.3/\beta' \\ 1.3\ , & t-t_0 > 1.3/\beta'\ , \end{cases}$$

where $\beta'=0.30$. The results of this experimental run are shown in Fig. 23. The plot in the lower left side shows $\dot{Q}/\dot{Q}_c$ (dashed curve) and $\Delta T/\Delta T_c$ (solid curve) as functions of time. Due to the nature of the run, the ramp rate β varies substantially immediately before the onset of convection. Therefore, we have not associated a value of β with this run. Measurements of $j^{\text{conv}}(t)$ are plotted in the lower right side. Unfortunately, measurements of $j^{\text{conv},g}(t)$ were not made. Therefore, the convective heat current is an estimated based on Eq. (3.6), and not the corrected current given by Eq. (3.7). Problems exist with these measurements (for example, the spike at $t\approx -1.5$ and the increase in j^{conv} afterwards), so we have not compared them with predictions of the amplitude equation. The problems are probably due to transients occurring after the abrupt ending of the increase in $\dot{Q}$ which would invalidate our method of calculating j^{conv}. The measurements do, however, clearly show the onset of convection

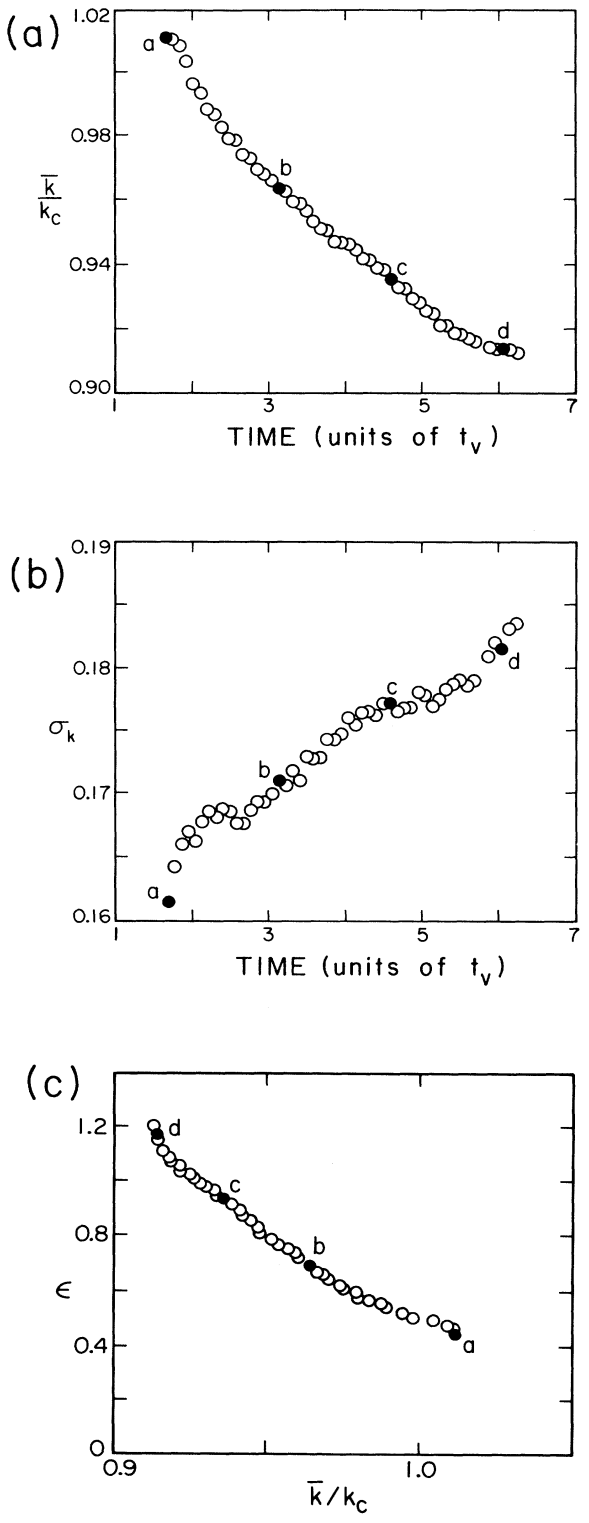

FIG. 22. Wave-number studies of the pattern evolution shown in Fig. 20. The solid circles refer to the images in that figure. (a) The average wave number $\bar{k}$ divided by k_c as a function of time. (b) The standard deviation σ_k of k from $\bar{k}$, divided by k_c, as a function of time. (c) The relation between $\bar{k}$ and ϵ during the experimental run.

at $t \approx 2$. The images taken during this experimental run are shown above the plots in Fig. 23. The times at which images (a), (b), and (c) were taken are indicated by the solid circles in the plot of $j^{\text{conv}}(t)$. The pattern is cellular when it first emerges, and yet heals to a roll-like pattern, even though ΔT no longer increases rapidly with time. Image (d) was obtained at $t \approx 38$, and shows that the pattern eventually heals to a near-perfect straight-roll pattern with grain boundaries on its sides. We observed that initial patterns in this cell frequently evolved to a perfect or near-perfect straight-roll pattern, in agreement with studies on long-term time evolution of convective structures [72,73]. We have not, however, made studies of the very-long-term evolution of straight-roll patterns in this cell to observe whether the time dependence found near the threshold in larger aspect ratio cells [73] would occur.

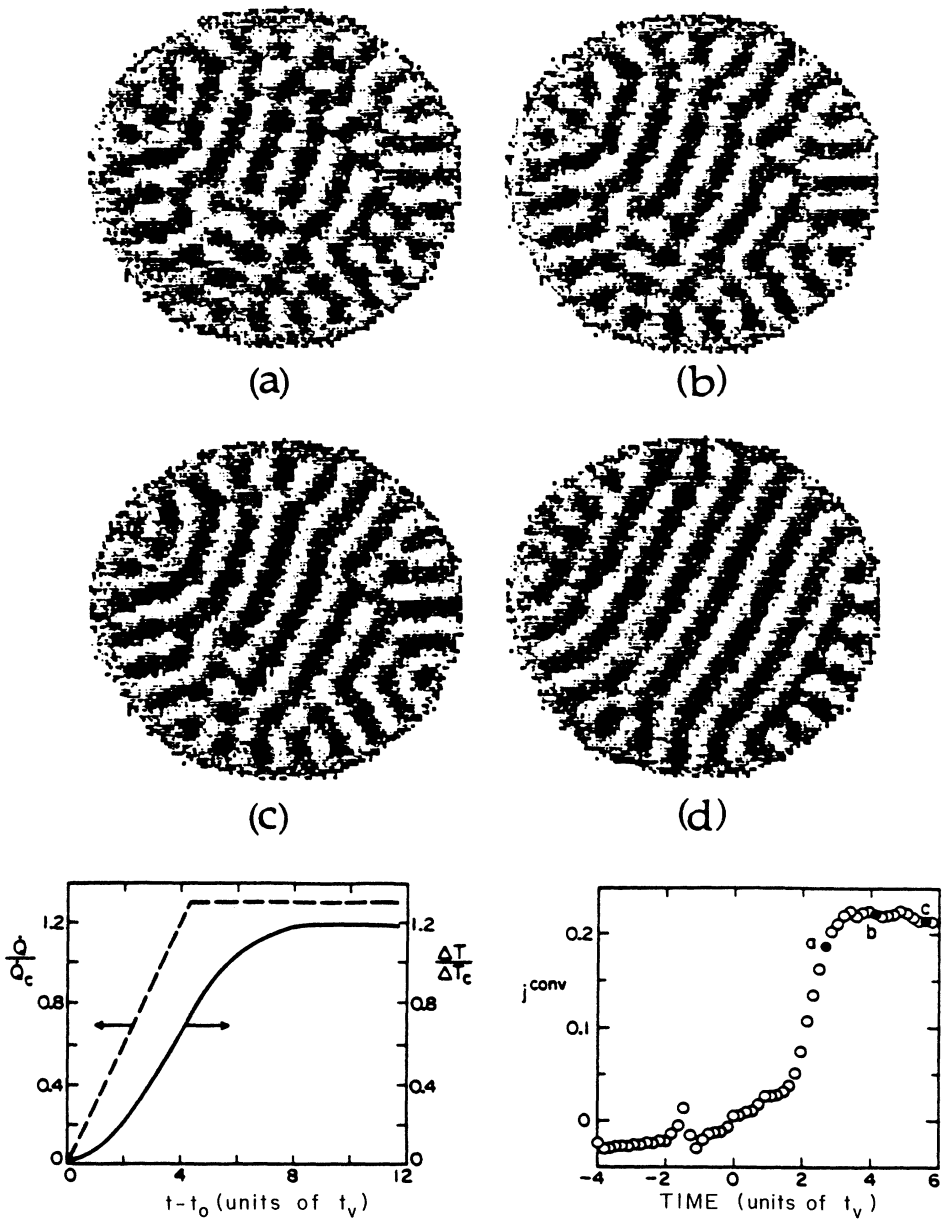

FIG. 23. Images (unfiltered) and heat-flux data from an experiment where the heat current was ramped initially with heating ramp rate $\beta' = 0.3$ until $\dot{Q}/\dot{Q}_c = 1.3$, after which the heat current was held at a constant value. Left-side plot: $\dot{Q}/\dot{Q}_c$ (dashed curve) and $\Delta T/\Delta T_c$ (solid curve) as a function of $t - t_0$. Right-side plot: The convective heat flux j^{conv} as a function of time. Solid circles correspond to points where images were taken. Image d was taken at $t \approx 38$.

D. Search for an experimental noise source

The best-fit values for $\bar{F}_{\text{expt}}$ or F_{expt} in the stochastic models are larger than the theoretical predictions for thermal noise given in Sec. IV by a factor of about 2×10^4. Because of this, we searched for apparatus-induced noise sources which could be responsible for these relatively large field intensities. We felt that the most likely source of apparatus-induced noise was the presence of temperature fluctuations in the sapphire top plate due to our temperature-regulation method. The temperature-controlled bath typically had variations of ≈0.5 mK, and the temperature immediately above the sapphire plate fluctuated by even larger amounts when a heat current passed through the cell. Variations with time of ≈6 mK were observed in the bath just above the sapphire plate when a steady heat current of $\dot{Q}_c$ was applied to the bottom plate of the cell. Since the sapphire plate was only 0.318 cm thick and had a finite, albeit large, conductivity, the pattern-formation process might have been influenced by these fluctuations.

We tested this hypothesis by replacing the sapphire plate with the top laminated from copper and acrylic. With this arrangement, the fluctuations were filtered by the low thermal diffusivity of the acrylic, and the high thermal conductivity of the copper plate below the acrylic but above the fluid insured that the temperature at the upper boundary of the fluid was virtually uniform and time independent. Flow visualization was no longer possible, but we could make heat-flux measurements to see if the field intensities were reduced. We once again performed a set of ramping experiments with $0.01\leq\beta'\leq0.32$ and with a gel sidewall. The resulting values of F_{expt} were already given in Figs. 16(a) and 16(b) as solid circles. There is no measurable difference between these data and the open squares, which correspond to the runs with the sapphire top and the gel sidewall. The results of this comparison show that the large fields we observed in our ramping experiments were not due to temperature fluctuations of the sapphire plate. We do not know of any other possible experimental source of the large values of the fields that we measured.

VI. SUMMARY

In this paper we have presented the results of an experimental investigation of the convective onset which occurs when the Rayleigh number R is ramped smoothly in time from below to above its critical value. We showed that an ordinary sidewall, with a thermal diffusivity different from that of the fluid, will induce a roll-like pattern which reflects the shape of the container. This is the case even when an appropriately scaled dimensionless ramp rate of R is as small as 0.01.

We were able to match very closely the thermal diffusivity of the wall and the fluid by using water for the convecting liquid, and by making the wall of a gel which contained primarily water but nonetheless was sufficiently rigid to maintain its shape in the presence of gravity and of fluid flow adjacent to it. With this sidewall, the convecting pattern which emerged differed dramatically from the sidewall-forced pattern. It consisted of randomly positioned cells which had no noticeable relationship to the geometry of the wall, and which were irreproducible from one experimental run to the next. Similar, seemingly random, patterns were obtained with sidewalls of circular and of square cross section.

We compare the convectively transported heat current with calculations based on three different models. One of these was a single-mode amplitude equation with a deterministic field. In fitting the solution of this equation to the data, only the field value had to be adjusted. This model gave a reasonable fit to the data at large ramp rates, but provided an unsatisfactory fit to the data with the gel sidewall at small ramp rates. When the deterministic field was replaced by a stochastic variable with Gaussian correlations, the fit was somewhat improved for low ramp rates, but was still not satisfactory. The stochastic Swift-Hohenberg model gave very similar results. We attribute the discrepancy between the data and the results of the stochastic models to experimental error in determining ΔT when using a sapphire top. When this top was replaced by one made of copper (which has even higher thermal conductivity than sapphire), an essentially perfect fit to the data was achieved with both stochastic models. The deterministic model still gave an inferior fit at the small ramp rates.

We believe that the random nature and the irreproducibility from run to run of the patterns, as well as the much better fit of the stochastic models to the convected current, are strong evidence for the stochastic nature of the convective onset when sidewall forcing is sufficiently weak. However, the intensity of the stochastic field required in the models to explain the experimental time evolution of the currents is a factor of about 2×10^4 larger than would be expected from the effect of the microscopic thermal motion in the fluid. We investigated the most likely source of experimental noise in our apparatus by replacing the sapphire cell top with a copper plate, thereby reducing dramatically the experimentally provoked thermal fluctuations at the top of the convection cell. This had no measurable effect on the measured field intensities, but, as discussed above, it did result in heat-current data which agreed very well with either stochastic model. We do not know whether the large field values are attributable to unknown deficiencies in the models or in the experiments. We note, however, that good agreement between experiment and theory has been found for fluctuations well away from bifurcations [74], as well as just below the bifurcation to electroconvection in nematic liquid crystals [75].

We also studied the evolution of the pattern at large times. The initially cellular patterns obtained with the gel wall evolved towards a pattern consisting primarily of straight or slightly curved rolls. We report measurements of the length of the boundary between regions of up-flow and down-flow, of the mean wave number, and of the variance of the wave number, during this process.

ACKNOWLEDGMENTS

We are grateful to Giovanni Dietler and Roger Drake for their help in preparing our gels, and to P. C. Hohen-

berg for numerous stimulating discussions. This work was supported by the U.S. Department of Energy under Grant No. DE-FG03-87ER13738. One of us (G.A.) is grateful to the Alexander von Humboldt Foundation for support, and would like to thank the University of Bayreuth for its hospitality while part of this paper was being written.

APPENDIX: METHOD OF DETERMINING BLACK-WHITE BOUNDARY LENGTH IN AN IMAGE

We present here a method for determining the total boundary length between black and white regions in images displayed with two grey levels (such as those shown in Fig. 21). All 2×2 matrices of adjacent pixels are examined. Each pixel is a part of four such matrices. Each matrix is one of sixteen different types, and each of these types can be placed in four major categories. Examples of these four categories are illustrated as (a), (b), (c), and (d) in Fig. 24, where black pixels are shown as shaded. In (a), all four pixels are the same, so no interface between black and white regions exists within the matrix. There are two matrix types in this category. In (b), two pixels are black, and two are white, and the boundary between the two regions is either vertical or horizontal. Four types of matrices exist in this category. The matrices in category (c) have three pixels of one shade and one pixel of the other shade. These matrices may contain part of a "staircaselike" diagonal border; otherwise, they contain a corner merging a horizontal boundary with a vertical one. This category is composed of eight matrix types. Finally, in (d), the matrix has two black pixels and two white pixels, but identical pixels are diagonally across from each other. It contains the intersection between two black regions and two white regions. There are two diagonal boundaries in the matrix; their orientation, however, is arbitrary. Two matrix types belong in this category.

Each 2×2 matrix involving an interface contains a unique segment of the total boundary. Each segment is assigned a length in pixel units. The total boundary length is determined by adding all these segment lengths together.

The matrices of category (a) do not involve an interface, so they are not included in the measurement. Those in category (b) contain a segment that is vertical or horizontal (the segments are illustrated by the heavy solid lines in Fig. 24). The length of this segment (in pixel units) is 1.0. The segments within the matrices of category (c) are defined to be diagonal with a length of $\sqrt{2}/2$. (If a matrix in this category actually contains a corner of the boundary, then the corner is made slightly rounded.) Finally, the matrices of category (d) contain two diagonal segments, each of length $\sqrt{2}/2$, and both of these lengths are added to the sum. Note that it is ambiguous where the segments should be located in the matrices of (d), so their placement is arbitrary. Nevertheless, the two segment lengths are independent of this placement.

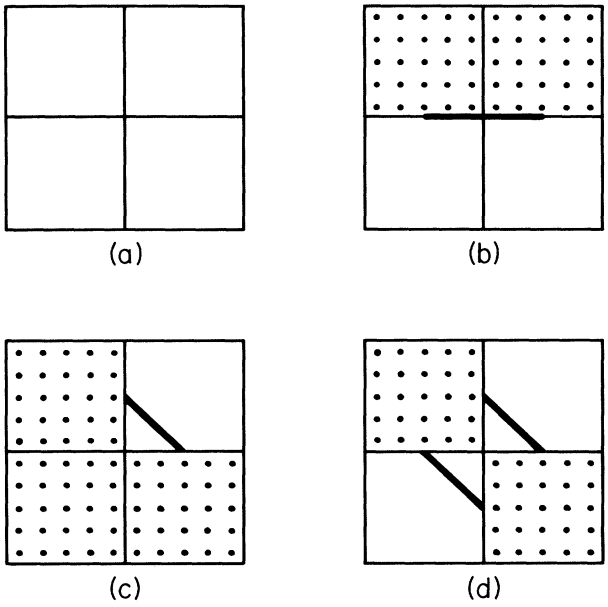

FIG. 24. Illustration of the categories of matrices that occur in the determination of the boundary lengths of images (see text).

We tested this method by measuring the perimeter of a circle bounding a black region from a white region. The radius of the circle ranged from 10 to 60 pixel units. For this range, the perimeter was consistently measured to be $\approx6\%$ greater than its correct value.

We normalized the boundary length by multiplying it by $\bar{\lambda}/2A_i$, where $\bar{\lambda}$ is the characteristic wavelength of the pattern and A_i is the area of the image, and both $\bar{\lambda}$ and A_i are given in pixel-length units. The wavelength $\bar{\lambda}$ was determined from a measurement of $\bar{k}$ in the Fourier transform of the image (see Sec. II D). The images shown in Fig. 21 were from a 128×128 matrix, and the area within which the border was actually measured was equivalent to that inside a 127×127 matrix, so $A_i=16\,129$.

As an example, consider an image containing a vertical straight-roll pattern with wavelength λ. Let the image be composed of an $L\times L$ matrix. Then there will be $2L/\lambda$ vertical boundaries of length L, making the total boundary length $B=2L^2/\lambda$. After normalization $B=1$. We tested this method on several images of nearly straight-roll patterns. In all cases we measured $B\approx0.95$.

[1] For numerous examples and references, see, for instance *Cellular Structures in Instabilities*, edited by J. E. Wesfreid and S. Zaleski (Springer, New York, 1984); or P. C. Hohenberg and J. S. Langer, J. Stat. Phys. **28**, 193 (1982); or G. Ahlers, in *Lectures in the Sciences of Complexity*, SFI Studies in the Sciences of Complexity, Vol. I, edited by D. Stein (Addison-Wesley Longman, New York, 1989), p. 175.

[2] H. Bénard, Rev. Gen. Sci. Pure Appl. **11**, 1261 (1900); **11**, 1309 (1900); Ann. Chim. Phys. **23**, 62 (1901).

[3] A large literature pertaining to this field has evolved. Particularly useful as introductions to early work are the reviews by E. L. Koschmieder, Adv. Chem. Phys. **26**, 177 (1974); and in *Order and Fluctuations in Equilibrium and Nonequilibrium Statistical Mechanics,* Seventeenth International Solvay Conference, edited by G. Nicolis, G. Dewel, and J. W. Turner (Wiley, New York, 1981), p. 168; and by F. Busse, in *Hydrodynamic Instabilities and the Transition to Turbulence,* edited by H. L. Swinney and J. P. Gollub (Springer, Berlin, 1984), p. 97; and in Rep. Prog. Phys. **41**, 1929 (1978).

[4] G. I. Taylor, Philos. Trans. R. Soc. London Ser. A **223**, 289 (1923).

[5] A sizable literature now exists dealing with this system. A comprehensive review has been given by R. C. DiPrima and H. L. Swinney, in *Hydrodynamic Instabilities and Transitions to Turbulence,* edited by H. L. Swinney and J. P. Gollub (Springer, Berlin, 1981). Important early papers in this field are numerous, but particulary noteworthy are D. Coles, J. Fluid Mech. **21**, 385 (1965); H. A. Snyder, *ibid.* **35**, 273 (1969); J. E. Burkhalter and E. L. Koschmieder, Phys. Fluids **17**, 1929 (1974).

[6] See, for instance, I. Rehberg, B. L. Winkler, M. de La Torre-Juarez, S. Rasenat, and W. Schöpf, Festkörperprobleme-Adv. Solid State Phy. **29**, 35 (1989).

[7] See, for instance, J. S. Langer and H. Müller-Krumbhaar, Acta Metall. **26**, 1681 (1978); **26**, 1689 (1978); **26**, 1967 (1978).

[8] See, for instance, G. I. Sivashinsky, Annu. Rev. Fluid Mech. **15**, 179 (1983).

[9] See, for instance, C. Vidal and A. Pacault, in *Evolution of Order and Chaos,* edited by H. Haken (Springer, Berlin, 1982).

[10] See, for instance, Proceedings of the Conference on Nonlinear and Chaotic Transport Phenomena in Semiconductors [Appl. Phys. A **48**, 93 (1989)].

[11] H. Risken and H. D. Vollmer, Z. Phys. **201**, 323 (1967).

[12] H. Risken, in *Progress in Optics,* edited by E. Wolf (North-Holland, Amsterdam, 1970), Vol. VIII, p. 239.

[13] F. T. Arecchi, G. S. Rodari, and A. Sona, Phys. Lett. **25A**, 59 (1967).

[14] F. T. Arecchi, M. Giglio, and A. Sona, Phys. Lett. **25**, 341 (1967).

[15] V. M. Zaitsev and M. I. Shliomis, Zh. Eksp. Teor. Fiz. **59**, 1583 (1970) [Sov. Phys.—JETP **32**, 866 (1971)].

[16] R. Graham, Phys. Rev. A **10**, 1762 (1974).

[17] J. B. Swift and P. C. Hohenberg, Phys. Rev. A **15**, 319 (1977).

[18] G. Ahlers, M. C. Cross, P. C. Hohenberg, and S. Safran, J. Fluid Mech. **110**, 297 (1981). There is an inconsistency between Eqs. (2.5) and (2.7) of this reference. The coefficient g in (2.7) should be replaced by $\bar{g}=3g_3/2$, according to the normalization given in (2.6), which ensures that $\langle \psi^2 \rangle = \langle A^2 \rangle$. Similarly, the coefficient g_5 of Eq. (4.1a) of the present paper yeilds $\bar{g}_5 = 5g_5/4$.

[19] H. S. Greenside and W. M. Coughran, Jr., Phys. Rev. A **30**, 398 (1984).

[20] A. Dougherty, P. H. Kaplan, and J. P. Gollub, Phys. Rev. Lett. **58**, 1652 (1987).

[21] S. Chandrasekhar, *Hydrodynamic and Hydromagnetic Stability* (Oxford University Press, London, 1961).

[22] A. Schlüter, D. Lortz, and F. Busse, J. Fluid Mech. **23**, 129 (1965).

[23] See, for instance, V. Steinberg, G. Ahlers, and D. S. Cannel, Phys. Scr. **32**, 534 (1985).

[24] M. C. Cross, P. C. Hohenberg, and M. C. Lücke, J. Fluid Mech. **136**, 169 (1983).

[25] J. B. Swift, P. C. Hohenberg, and G. Ahlers, Phys. Rev. A **43**, 6572 (1991).

[26] P. C. Hohenberg and J. B. Swift (unpublished).

[27] C. W. Meyer, G. Ahlers, and D. S. Cannell, Phys. Rev. Lett. **59**, 1577 (1987).

[28] G. Ahlers, C. W. Meyer, and D. S. Cannell, J. Stat. Phys. **54**, 1121 (1989).

[29] D. S. Cannell, C. W. Meyer, and G. Ahlers, in *1988 ASI Random Fluctuations and Pattern Growth: Experiments and Theory* (Kluwer, Dordrecht, 1988).

[30] F. Busse, J. Fluid Mech. **30**, 625 (1967); and references therein.

[31] G. Ahlers, J. Fluid Mech. **98**, 137 (1980).

[32] This information was provided by Cascade Designs.

[33] D. S. Cannell (private communication).

[34] H. R. Haller, C. Destor, and D. S. Cannell, Rev. Sci. Instrum. **54**, 973 (1983).

[35] P. L. Silveston, Forsch. Geb. Ingenieur Wes. **24**, 29 (1958).

[36] For a description of early work by Silveston (Ref. [35]), see Sec. II.18 of Chandrasekhar (Ref. [21]).

[37] M. M. Chen and J. A. Whitehead, J. Fluid Mech. **31**, 1 (1968).

[38] See, for instance, F. H. Busse and J. A. Whitehead, J. Fluid Mech. **66**, 67 (1974).

[39] D. R. Jenkins, J. Fluid Mech. **190**, 451 (1988).

[40] S. Rasenat, G. Hartung, B. L. Winkler, and I. Rehberg, Experiments in Fluids **7**, 412 (1989).

[41] M. A. Dominguez-Lerma, G. Ahlers, and D. S. Cannell, Phys. Fluids **27**, 856 (1984).

[42] R. P. Behringer and G. Ahlers, J. Fluid Mech. **125**, 219 (1982).

[43] A. Oberbeck, Ann. Phys. Chem. **7**, 271 (1879).

[44] J. Boussinesq, *Théorie Analytique de la Chaleur,* (Gauthier-Villars, Paris, 1903), Vol. 2.

[45] C. W. Meyer, Ph.D. dissertation, Department of Physics, University of California at Santa Barbara, 1988.

[46] G. Ahlers, Phys. Rev. Lett. **33**, 1185 (1974).

[47] R. P. Behringer and G. Ahlers, Phys. Lett. **62A**, 329 (1977).

[48] R. W. Walden and G. Ahlers, J. Fluid Mech. **109**, 89 (1981).

[49] S. Ciliberto, E. Pampaloni, and C. Perez-Garcia, Phys. Rev. Lett. **61**, 1198 (1988).

[50] L. D. Landau and E. M. Lifshitz, Fluid Mechanics (Addison-Wesley, Reading, MA, 1959).

[51] H. van Beijeren and E. G. D. Cohen, J. Stat. Phys. **53**, 77 (1988).

[52] H. van Beijeren and E. G. D. Cohen, Phys. Rev. Lett. **60**, 1208 (1988).

[53] J. N. Schaumeyer, R. P. Behringer, and R. Baierlein, J. Fluid Mech. **109**, 339 (1981).

[54] W. H. Press, B. P. Flannery. S. A. Teukolsky, and W. T. Vetterling, *Numerical Recipes, The Art of Scientific Computing* (Cambridge University Press, Cambridge, England, 1986).

[55] We used the functions gasdev() and ran3() of Press *et al.*, [54] to generate a Gaussian random variable. We tested our procedure for the linear equation ($g_3=g_5=0$) with $\epsilon<0$ where the steady-state solution is $\langle A^2 \rangle = -\bar{F}/\epsilon$.

Averaging 10^4 integrations, our numerical result agreed with the analytic value within about 1%. Similar agreement was obtained also with the function ran1(); but the use of ran0() with gasdev(), which requires the local random-number generator, gave results which for some parameter values were in error by over 10% even though the moments of the distribution function agreed with the expected values as well as could be expected.

[56] This value differs slightly from that provided in early publications [27–29]. Previously, the approximate solution to Eq. (4.3) of ACHS [18] had been used, whereas in the present paper we integrated Eq. (4.3) directly as described in Sec. IV B. As has been discussed recently by Swift *et al.* [25], the approximation of ACHS fails for $\epsilon<0$. Therefore it leads to inaccurate results for $\bar{F}_{\text{expt}}$ unless a particularly fortunate choice is made for t_0. None of the errors in the previously reported values of $\bar{F}_{\text{expt}}$ are large enough to have a significant influence on the interpretation of our work.

[57] R. Soberman, J. Appl. Phys. **29**, 872 (1958).

[58] E. L. Koschmieder, Beitr. Phys. Atmos. **39**, 1 (1966).

[59] C. Q. Hoard, C. R. Robertson, and A. Acrivos, Int. J. Heat Mass Transfer **13**, 849 (1970).

[60] E. F. C. Somerscales and T. S. Dougherty, J. Fluid Mech. **42**, 755 (1970).

[61] To avoid the problems at small ramp rates mentioned above, only the data near the early evolution to macroscopic values of j^{conv} were used in the fits.

[62] We note that the definition of $\bar{f}$ used by ACHS differs from that of our f_{Det} by a factor of τ_0, so that $\tau_0\bar{f}_{\text{ACHS}}=f_{\text{Det}}$. We also note a typographical error in the captions of Figs. 13 and 14 of ACHS, where $\bar{f}^0$ should have been quoted as 7×10^{-4}. The correct value was used to compute the curves in their Fig. 14.

[63] P. G. Daniels, Proc. R. Soc. London Ser. A **358**, 173 (1977).

[64] Useful data sources are *Modern Plastics Encyclopedia,* edited by Joan Agranoff (McGraw-Hill, New York, 1982), Vol. 59, p. 483; and *Encyclopedia of Polymer Science and Technology* (Interscience Publishers, New York, 1966).

[65] The value of "$\cos(\alpha)$" in Eq. 38 of Ref. [24] was set to unity when we obtained this value of f_1 (see discussion at the end of Ref. [24]).

[66] R. E. Kelly and D. Pal, J. Fluid Mech. **86**, 433 (1978).

[67] P. Hall and I. C. Walton, Proc. R. Soc. London Ser. A **358**, 199 (1977).

[68] E. L. Koschmieder and S. G. Pallas, Int. J. Heat Mass Transfer **17**, 991 (1974), and references therein.

[69] S. G. Pallas, Ph.D. dissertation, College of Engineering, University of Texas, 1972.

[70] E. L. Koschmieder, Adv. Chem. Phys. **26**, 177 (1974); and references therein.

[71] A. Pocheau and V. Croquette, J. Phys. **45**, 35 (1984).

[72] M. S. Heutmaker, P. N. Frenkel, and J. P. Gollub, Phys. Rev. Lett. **54**, 1369 (1985); and references therein.

[73] G. Ahlers, D. S. Cannell, and V. Steinberg, Phys. Rev. Lett. **54**, 1373 (1985).

[74] B. M. Law, P. N. Segrè, R. W. Gammon, and J. V. Sengers, Phys. Rev. A **41**, 816 (1990).

[75] I. Rehberg, S. Rasenat, M. de la Torre-Juarez, W. Schöpf, F. Hörner, G. Ahlers, and H. R. Brand, Phys. Rev. Lett. (to be published).